Journal of Rock Mechanics and Geotechnical Engineering 18 (2026) 3916–3933

Contents lists available at ScienceDirect

Journal of Rock Mechanics and Geotechnical Engineering

journal homepage: www.jrmge.cn

Full Length Article

A nonlinear unified hardening model for breakable siliceous mudstone coarse-grained soil under low confining pressure considering penetrating erosion

Ling Zhang [a,b,c], Yunhao Chen [a], Xuzhen He [d,*], Shaoheng Dai [d], Biao Luo [a], Daichao Sheng [d]

[a] College of Civil Engineering, Hunan University, Changsha, 410082, China
[b] Key Laboratory of Building Safety and Energy Efficiency of the Ministry of Education, Hunan University, Changsha, 410082, China
[c] National International Joint Research Center for Building Safety and Environment, Hunan University, Changsha, 410082, China
[d] School of Civil and Environmental Engineering, University of Technology Sydney, Sydney, 2007, Australia

ARTICLE INFO

Article history:
Received 2 March 2025
Received in revised form
30 May 2025
Accepted 5 June 2025
Available online 4 September 2025

Keywords:
Penetrating erosion
Particle breakage
Critical state
Breakable coarse-grained soil (SMCGS)
Unified hardening constitutive (UH)

ABSTRACT

The stress–strain behavior of brittle siliceous mudstone coarse-grained soils (SMCGSs) under penetrating erosion critically affects the stability of SMCGS-filled embankments in erosion-prone areas, yet remains insufficiently understood, particularly regarding particle crushing and critical state behavior under low confining pressures. This study proposes a modified constitutive model to characterize erosion-induced mechanical degradation and nonlinear critical state evolution. A normalized parameter ϑ, derived from the principle of crushing equivalence, is introduced to capture the coupled effects of particle breakage and critical state shifts under varying erosion intensities. Along with a nonlinear tuning index δ, this parameter is integrated into the unified hardening model for low confining pressure (UH-L), resulting in the N-UH-LE model. Consolidated drained (CD) triaxial tests under confining pressures of 100–400 kPa are conducted for model calibration and validation. The model predictions exhibit strong agreement with experimental results, with a maximum relative error of 7.76 %. The N-UH-LE model successfully reproduces key mechanical responses, including hardening, softening, shear dilation, and volumetric changes across different erosion levels. Furthermore, erosion-induced degradation decreases with lower confining pressures and higher initial void ratios (e_0 = 0.3, 0.5, and 0.7), while variations in interlocking strength ($\tau_0 \cot\varphi$ = 40 kPa, 80 kPa, and 120 kPa) show limited influence.

1. Introduction

Brittle siliceous mudstone coarse-grained soils (SMCGSs), commonly generated by excavation and tunneling, have become important supplementary materials for embankment filling due to their availability and suitability for engineering applications (Li et al., 2017). However, SMCGS generally exhibits low structural cohesion due to weakened cementation among particles (Aziz et al., 2016; Israr and Aziz, 2019; Rasool and Aziz, 2020; Zhou et al., 2022). Progressive weathering causes mineral dissolution and incorporation of clay minerals, resulting in decreased density and hardness (Aziz et al., 2024; Xu et al., 2024; Zou et al., 2025). As a result, SMCGS becomes increasingly porous and mechanically vulnerable under low confining pressures typical of embankment applications (10 kPa–1 MPa) (Peng et al., 2020; Xiao et al., 2019; Wu et al., 2024; Liu et al., 2020), which further exacerbates susceptibility to moisture infiltration, swelling, and softening (Crowell, 1957; Hu et al., 2017; Zeng et al., 2024; Dai et al., 2023). Moreover, water–soil interactions further induce fine particle depletion, resulting in meso-structural alterations and degraded mechanical properties, including increased void ratio and hydraulic conductivity, and diminished shear strength and structural stability (Aziz et al., 2010; Ma et al., 2021; McKenna et al., 2021; Zhang and Liu, 2023; Peng et al., 2024). Therefore, it is critical to develop a modified constitutive model that accounts for penetrating erosion effects on SMCGS, particularly focusing on particle crushing and critical state behavior

* Corresponding author.
E-mail address: xuzhen.he@uts.edu.au (X. He).
Peer review under responsibility of Institute of Rock and Soil Mechanics, Chinese Academy of Sciences.

https://doi.org/10.1016/j.jrmge.2025.06.028

under low confining pressures (Liu et al., 2021, 2022; Xu et al., 2022).

The unified hardening (UH) models, derived from the improved Modified Cam–Clay (MCC) framework, have been widely employed to simulate the complex mechanical response of overconsolidated soils, accurately reproducing stress–strain behaviors under various loading conditions (Yao et al., 2009, 2019; Yao and Kong, 2012). The UH sand model, in particular, captures yielding, hardening, and softening with fewer physically meaningful parameters while retaining MCC model fundamentals (Yao et al., 2014, 2017; Zheng, 2015). Particle crushing significantly influences soil critical states (Sheng et al., 2008), prompting integration of particle breakage parameters into UH models for sands. However, these formulations were calibrated for high-stress regimes, leaving their applicability to brittle SMCGS at low confining pressures unverified. Recent studies introduced crushing parameters and optimization algorithms to model critical state lines under varied breakage degrees (Xiong et al., 2021), while the UH-L model incorporated locking strength and nonlinear friction angle dependence on confining stress for coarse-grained soils at low pressures (Yao and Fang, 2020). Nevertheless, nonlinear critical state responses under low confining pressures and erosion effects remain unaddressed (Liu et al., 2025).

In addition to mechanical loading (Shi et al., 2022; Yu, 2017; Zhao et al., 2025a, 2025b), UH frameworks have been further extended to account for extrinsic factors such as temperature, time, and matric suction (Yao and Zhou, 2013; Yao and Fang, 2020; Yao et al., 2024). However, a constitutive model that explicitly incorporates the effects of penetrating erosion on coarse-grained soils remains undeveloped (Li et al., 2025; Yang et al., 2020).

To overcome this limitation, this study develops a nonlinear UH constitutive model for breakable SMCGS under low confining pressures by integrating the coupled effects of penetration-induced erosion and critical state nonlinearity. Two additional parameters are introduced into the UH-L model to form a modified model (N-UH-LE): a normalized interaction index (ϑ), capturing the coupled effects of particle crushing and critical state evolution induced by penetration erosion, and a nonlinear tuning coefficient (δ), characterizing critical state nonlinearity. The N-UH-LE model is calibrated and validated through consolidated drained triaxial tests conducted on both eroded and uneroded specimens. This work provides a robust numerical and theoretical foundation for assessing the stability and long-term performance of geotechnical structures such as high-speed rail subgrades, highway embankments, and reservoir slopes subjected to coupled mechanical and hydraulic loadings.

2. Impacts of penetrating erosion on SMCGS

Taking the consolidated drained (CD) triaxial experiments on SMCGS specimens treated by penetration erosion as an example (Chen et al., 2024), the penetrating erosion effects on the meso-structure and mechanical characteristics of SMCGS are investigated in this section.

2.1. Test review

The particle size distribution (PSD) of the designated SMCGS sample for the CD triaxial tests is presented in Fig. 1. The physical and mechanical properties are demonstrated in Table 1.

The details for the suite of CD triaxial experiments conducted on SMCGS specimens with or without penetrating erosion treatment are demonstrated as follows.

The SMCGS specimens, prepared to the specified target moisture and relative density, were subjected to penetrating erosion

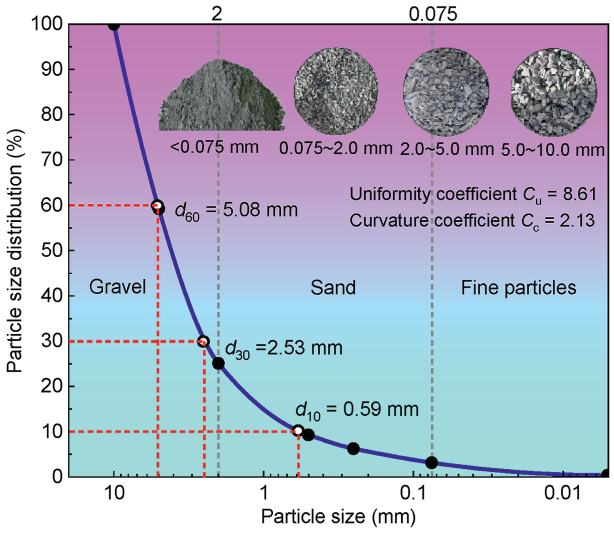

Fig. 1. Particle size distribution curve of SMCGS specimen.

treatment according to the apparatus illustrated in Fig. 2 (The device primarily consists of a water storage reservoir, a frequency conversion pump, an inverted funnel, a membrane-retaining cylinder, and associated water piping, with the pump enabling precise control of the penetrating erosion intensity ranging from 0 to 450 kPa). Specifically, the experiment steps involved placing two permeable stones (50 mm diameter, 5 mm thick) at the SMCGS specimen top and bottom within a rubber membrane, with a 10 μm pore-size filter paper inserted at the bottom to prevent fine particle loss and clogging (see Fig. 2). An inverted metal funnel connected the membrane-retaining cylinder to the water piping, sealed with binding tape. After activating the pump and adjusting the pressure, penetrating erosion was applied for 10 min when water emerged from the bottom permeable stone. After treatment, the penetrated specimens were allowed to be placed at room temperature, with weight measurements taken every 30 min. A high-precision electronic balance was employed to ensure accurate monitoring of moisture content. After each weighing, the mass of each specimen was recorded, ensuring that the specimen's mass remained stable across multiple measurement until it aligned with the initial moisture content before the penetration erosion treatment. It can eliminate wetting effects and isolate the mechanical influence of particle reallocation caused by penetrating erosion.

The penetration erosion intensity (pressure) involved above can be determined according to Eq. (1). During heavy to torrential events, rainfall rates over a 12-h span range from 4.1667 mm/h to 8.7417 mm/h. By Eq. (1), these values correspond to penetrating erosion pressures of 40.833–85.668 kPa, from which four levels (i.e. 40 kPa, 50 kPa, 60 kPa, and 70 kPa) were chosen (Chen et al., 2025).

$$p_0 = \rho_w g \frac{\eta \cdot I \cdot t}{K} \tag{1}$$

where p_0 denotes the penetrating erosion intensity (kPa); ρ_w refers to the water density (1000 kg/m^3); g represents the gravitational acceleration (9.81 m/s^2); I indicates the rainfall intensity (mm/h); t specifies the rainfall duration (12 h); η reflects the effective infiltration ratio (0.7 in this investigation); and K corresponds to the permeability coefficient of SMCGS specimen, found to be about 0.008409 m s^{-1}.

After penetrating erosion, the CD triaxial experiments were

Table 1
Physical and mechanical indices of SMCGS specimens.

Maximum dry density, $\rho_{d\ max}$ (kg m^{-3})	Optimal moisture content, w_{op} (%)	California bearing ratio (CBR) (%)	Resilient modulus, E_0 (MPa)	Porosity, n_0 (%)	Liquid limit, w_L (%)	Plastic limit, w_P (%)	Plasticity index, I_P
2230	8.4	87.6	104.5	22.6	29.1	21	8.1

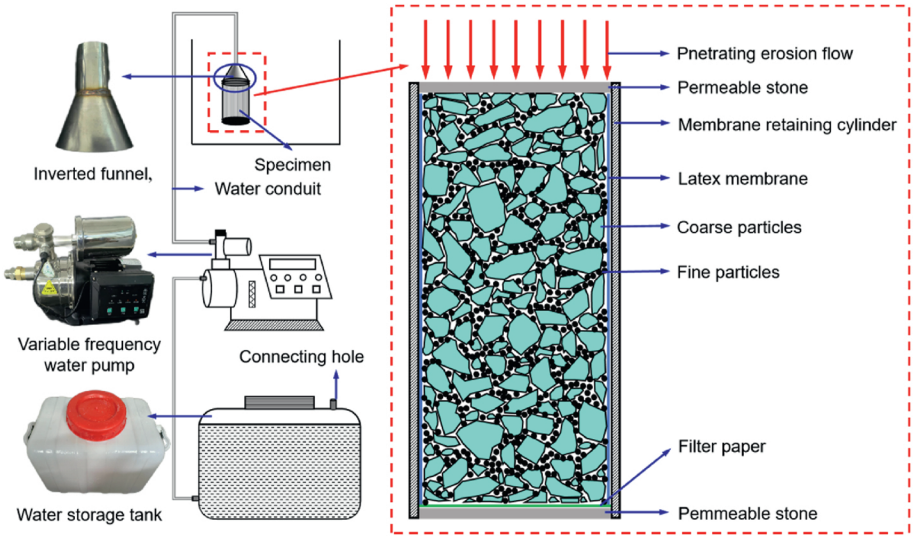

Fig. 2. Treatment schematic for penetration erosion.

carried out through the standard stress path triaxial apparatus (STDTTS). The test procedures are as follows. Specimens were backpressurized to achieve over 95 % saturation. Subsequently, four gradients of confining pressure (ranging from 100 kPa to 400 kPa) were applied, with volumetric changes tracked throughout consolidation. Once equilibrium was reached, triaxial shear experiments were conducted at a constant axial strain rate of 0.24 mm/min, terminating each run at 20 % axial strain. The loading settings are indicated in Table 2, and three parallel tests were performed for each setting. Meanwhile, a statistical analysis was performed on the particle gradation before and after loading. The details are as follows: mix the three compacted SMCGS specimens and the loaded parallel ones for each setting, separately, and then obtain their PSDs through air drying, grinding, and vibration screening. As a representative, Fig. 3 presents the deviatoric stress–shear strain (q–ε_d) and mean stress–volumetric strain (p–ε_v) curves, together with the PSD, for SMCGS specimens (both untreated and exposed to a 40 kPa penetration erosion intensity (p_0)) under varying confining pressures (σ_3).

2.2. Mesoscopic fabric

This section elucidates the mesoscopic fabric of SMCGS specimens under various penetrating erosion intensities. To assess the internal structural changes induced by erosion, both untreated and eroded specimens were scanned using a Phoenix v|tome x|s industrial CT system. Transverse XCT scan slices of untreated specimens (p_0 = 0 kPa) and those under two distinct penetration erosion intensities (p_0 = 40 kPa and 70 kPa) at various sites are demonstrated in Fig. 4. Referred to Tang and Gratchev (2023), the PCAS software was employed to analyze the slice images of specimens obtained from XCT scanning, extracting the porosity of each cross-section at 0.05 mm intervals, detailed in Fig. 5 (Note: The white area in Fig. 5b and the colored area in Fig. 5c are pores, and the color indicates the pore size). Consequently, the variation of interfacial voids along the specimen depth was obtained, as illustrated in Fig. 6.

As shown in Fig. 4a, in the absence of seepage erosion treatment, the particles are uniformly distributed, with clay particles densely packed within the pores of the particle skeleton, and the internal pore structure of the specimen predominantly consists of small pores (suspension-dense fabric). Upon application of p_0, the fine particles in the upper region migrate downward. Specifically, the sites closer to the penetrating source are more susceptible to the removal of fine particles by erosion, resulting in an increased void ratio in these regions. In contrast, those farther from the infiltration origin may exhibit a decrease in void ratio due to the deposition of fine particles. As depicted in Fig. 4b and c, the pore size in the upper section progressively expands with an increase in p_0 (e.g. at the site of h/10), while larger pores tend to develop

Table 2
Loading setting for CD triaxial experiments.

Test number	Testing type	Penetration erosion intensity, p_0 (kPa)	Confining pressure, σ_3 (kPa)
A1-A4	CD	0	100, 200, 300, 400
B1-B4		40	100, 200, 300, 400
C1-C4		50	100, 200, 300, 400
D1-D4		60	100, 200, 300, 400
E1-E4		70	100, 200, 300, 400

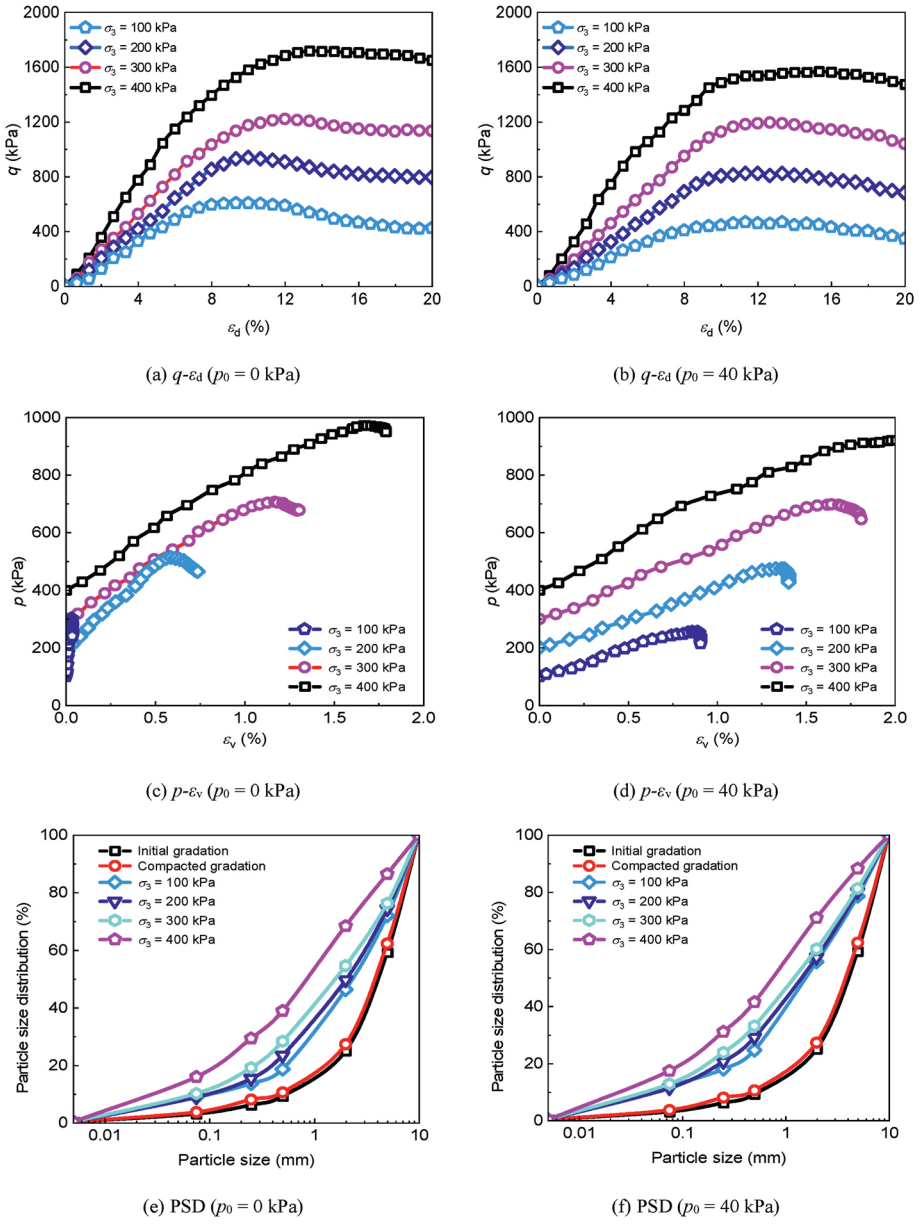

Fig. 3. The results of CD triaxial experiments on SMCGS with and without penetrating erosion.

further downward (e.g. at $p_0 = 40$ kPa, larger pores extend to $h/5$; at $p_0 = 70$ kPa, they extend to $3h/5$). It is noteworthy that penetrating erosion alters the redistribution of particles and pores without changing the average void ratio of the SMCGS specimens (see Fig. 6). It arises from the observation that there is no fine particle migration or significant volume change in the specimens subjected to penetrating erosion, owing to the constraints imposed by the membrane cylinder and filter paper.

In the absence of penetrating erosion, the coarse particles are uniformly and randomly distributed, with limited direct contact between them, as they are enveloped and filled by fine cohesive particles. The contact forces loaded on the coarse particles are uniformly distributed under triaxial loading, resulting in minimal fragmentation. After penetrating erosion, the upper fine particles migrate downward, leading to an increase in pores. The enlarged pores are compressed in the treated specimens subjected to triaxial loading, resulting in adaptive adjustments in the positions of the coarse particles, facilitating direct contact between them. Consequently, the forces acting on the coarse particles become concentrated, thereby increasing the likelihood of fragmentation (see Fig. 7). According to the previous discussion, it can be inferred that as the intensity of penetrating erosion increases, the degree of fragmentation in the upper portion of the SMCGS specimens becomes more pronounced under the triaxial loading. Therefore, it is feasible to consider crushing behavior as an intermediate hub to characterize the penetrating erosion impacts on the stress-strain responses of SMCGS (Li et al., 2021; Qian et al., 2024; Wei et al., 2018; Yao et al., 2022).

2.3. Normalized parameter (ϑ)

Particle breakage was characterized with improved relative breakage potential (B_r*), as proposed by Einav (2007) (see Fig. 8 and Eq. (2)), to compute B_r* for specimens sheared under the

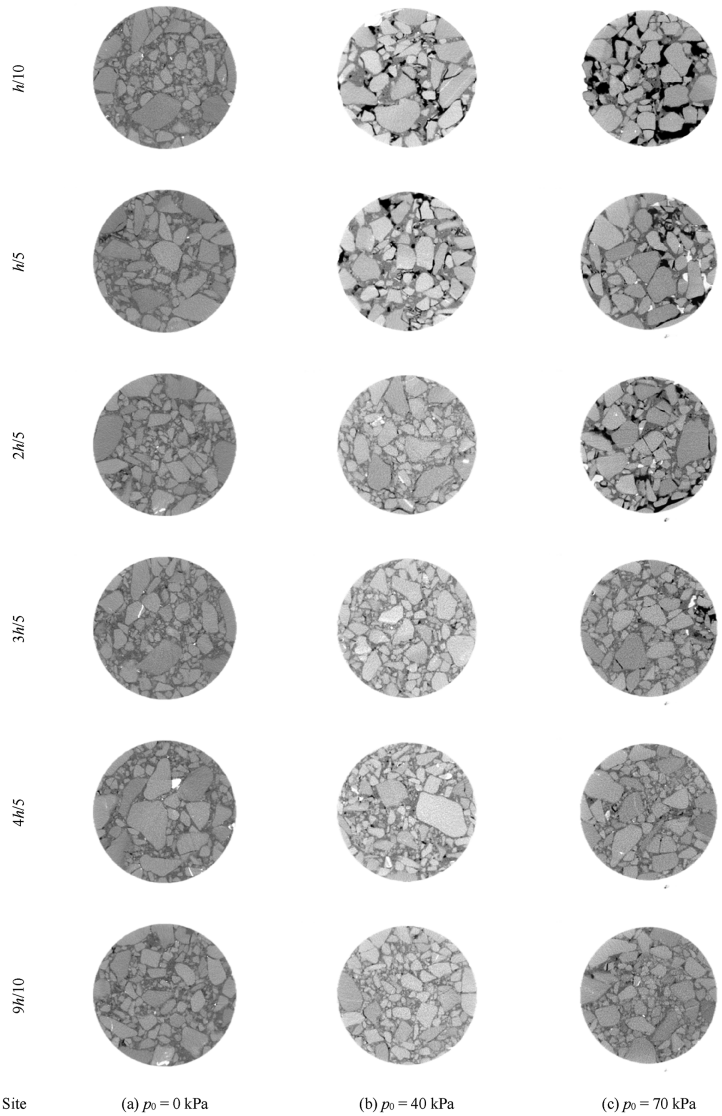

Fig. 4. XCT scan slices of both treated and untreated SMCGS specimens.

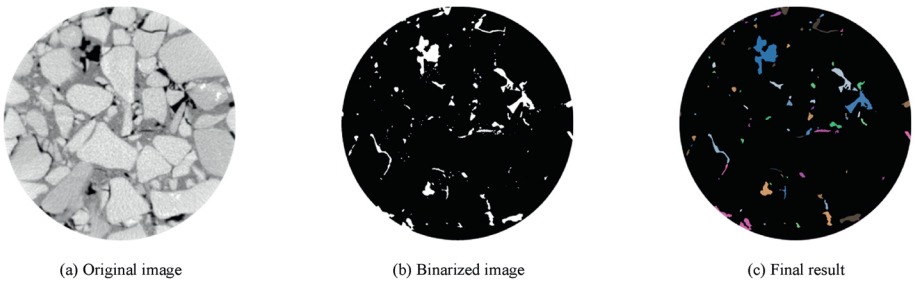

Fig. 5. Pore analysis images based on PCAS.

different test conditions.

$$B_r^* = \frac{B_p}{B_t} = \frac{\int_{d_m}^{d_M} (F(d) - F_0(d))\mathrm{d}(\log_{10} d)}{\int_{d_m}^{d_M} (F_u(d) - F_0(d))\mathrm{d}(\log_{10} d)} \quad (2)$$

where B_p is defined as the area between the compacted PSD ($F_0(d)$) and the post-crushing PSD ($F(d)$), while B_t corresponds to the area between $F_0(d)$ and the ultimate gradation curve $F_u(d)$. In this formulation, $F_0(d)$ and $F_u(d)$ denote the compacted and ultimate gradations, in that order; $F(d)$ signifies the instantaneous gradation during particle crushing at size d. Lastly, d_M and d_m specify the maximum and minimum particle sizes of the SMCGS specimen.

Energy expenditure occurs during particle breakage (Tang and Zhu, 2025), and the extent of the improved relative breakage potential (B_r*) correlates with the input plastic work (W_p) (Hu et al.,

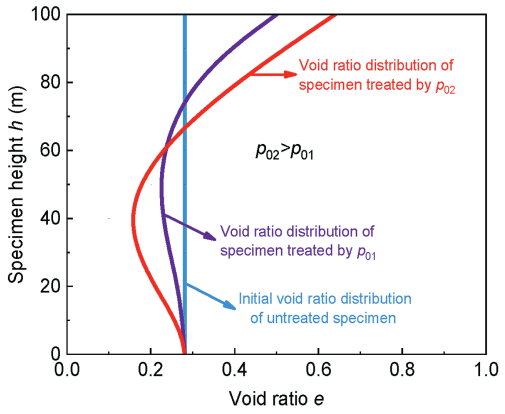

Fig. 6. Void ratio distribution across sections of SMCGS specimen under penetrating erosion.

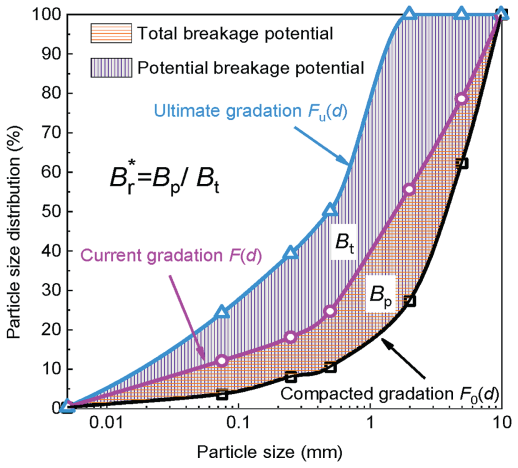

Fig. 8. Definition of improved relative breakage potential B_r*.

2011). Consequently, a W_p–B_r* correlation can be derived to characterize SMCGS particle breakage behavior, with W_p computed from Eq. (3) and Fig. 3a–d (Chen et al., 2025).

$$W_p = \int p\langle d\varepsilon_v^p\rangle + q d\varepsilon_d^p \tag{3}$$

where $d\varepsilon_v^p$ and $d\varepsilon_d^p$ represent the increments of plastic volumetric strain and plastic shear strain, in that order. When $d\varepsilon_v^p > 0$, $\langle d\varepsilon_v^p\rangle = d\varepsilon_v^p$; when $d\varepsilon_v^p < 0$, $\langle d\varepsilon_v^p\rangle = 0$.

Eq. (4) was formulated to characterize the integrated correlation between B_r* and $(W_p)^n$.

$$B_r^* = \frac{(W_p)^n}{\alpha + (W_p)^n} \tag{4}$$

where n and α refer to fitting parameter and material parameter, respectively.

Subject to varying penetrating erosion intensities, SMCGS exhibits differing strength–deformation characteristics and degrees of particle crushing. To establish a unified constitutive description, one can non-dimensionalize the macroscopic stress or plastic work by introducing parameters that capture the breakage resistance subjected to each erosion intensity, thereby collapsing the test data onto a common normalized framework.

It is postulated that two geometrically analogous specimens subjected to various erosion pressures reach equivalent particle-breakage states (Chen et al., 2025). Owing to identical particle morphology and gradation, SMCGS specimens exposed to different erosion pressures exhibit congruent macroscopic stress responses, as described by Eq. (5).

$$\frac{\sigma_{ijA}}{\vartheta_A} = \frac{\sigma_{ijB}}{\vartheta_B} \tag{5}$$

where σ_{ijA} and σ_{ijB} denote the macroscopic stress tensors for SMCGS under conditions A and B, while ϑ_A and ϑ_B are the stress-normalized parameters quantifying particle-breakage strength in those two scenarios.

Owing to the geometric similarity of specimens in scenarios A and B, their deformations under σ_{ijA} and σ_{ijB} are equivalent (Chen et al., 2025). By combining Eqs. (3) and (5), one obtains the formulation for plastic work under different penetrating erosion intensities, as presented in

$$\frac{W_{pA}}{\vartheta_A} = \frac{W_{pB}}{\vartheta_B} \tag{6}$$

where W_{pA} and W_{pB} are the input plastic work at various settings.

Given identical particle breakage under settings A and B, the improved relative breakage potential (B_r*) remains the same, which corresponds to the plastic work inputs W_{pA} and W_{pB} at their

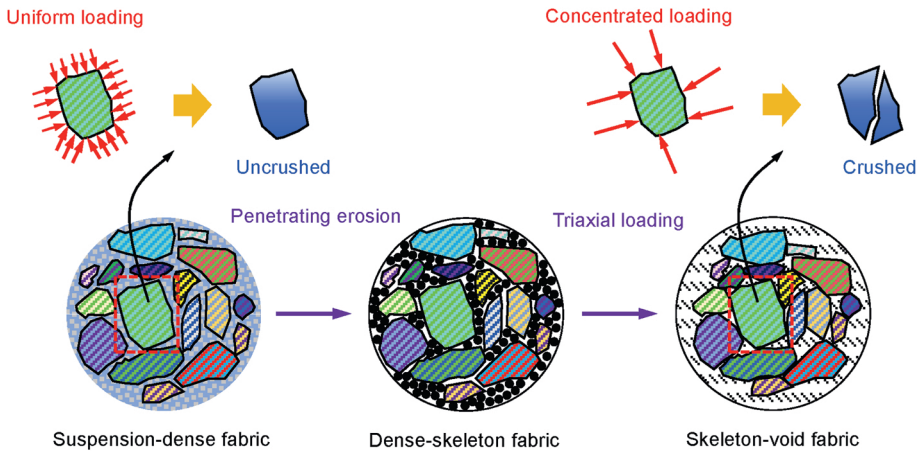

Fig. 7. Mesoscopic fabric changes in SMCGS specimen under penetrating erosion and triaxial loading.

respective erosion intensities. Consequently, Eq. (7) follows directly from

$$\frac{(W_{pA})^n}{\alpha_A + (W_{pA})^n} = \frac{(W_{pB})^n}{\alpha_B + (W_{pB})^n} \tag{7}$$

where α_A and α_B are the material parameters of Eq. (4) subjected to various settings.

Eq. (7) can be subsequently reconstituted as:

$$\frac{W_{pA}}{\alpha_A{}^{1/n}} = \frac{W_{pB}}{\alpha_B{}^{1/n}} \tag{8}$$

By integrating Eqs. (6) and (8), the normalized parameter ϑ is defined in Eq. (9):

$$\vartheta = \alpha^{1/n} \tag{9}$$

2.4. CSL in the p/ϑ - q/ϑ plane

By merging Eqs. (6) and (7) and introducing the normalized parameter ϑ, calibrated from triaxial-test particle-breakage statistics, relatively unified statistical trends for both particle breakage and critical-state behavior emerge in the normalized coordinate framework (Chen et al., 2025). Specifically, Fig. 9 depicts the CSL on the p/ϑ - q/ϑ plane. Evidently, the CSL behaves as a nonlinear curve that does not intersect the origin in the p/ϑ - q/ϑ space, characterized by Eq. (10). In detail, when the p approaches zero, the SMCGS specimens still retain a measurable shear strength, mainly owing to the interlocking effect between particles (Yao and Fang, 2020). Moreover, the nonlinear morphology of the CSL arises from the interplay of particle rearrangement, the nonlinear characteristics of inter-particle contact stiffness and friction, and shear dilatancy effects (Chen et al., 2025).

$$\frac{q}{\vartheta} = M\left(\frac{p + \tau_0 \cot\varphi}{\vartheta}\right)^{\delta} \tag{10}$$

where M is characterized by the critical stress state ratio; $\tau_0\cot\varphi$ refers to the interparticle locking strength stemming from the internal fabric of the super-consolidated SMCGS; δ is the nonlinear fine-tuning index describing the CSL morphology.

3. N-UH-LE model

In this section, the unified hardening (UH) model was selected as the foundational framework for this investigation due to its theoretical robustness and adaptability in capturing strain hardening/softening, dilation, and large-strain behavior grounded in critical state soil mechanics (Yao et al., 2009, 2019; Yao and Kong, 2012). Its modular structure allows for the incorporation of additional mechanisms, such as particle crushing and erosion-induced degradation, making it particularly suitable for modeling the complex behavior of SMCGSs affected by penetrating erosion under low confining pressures. Despite its advantages, the original UH model does not explicitly consider particle breakage, nonlinear critical state evolution under low pressures, or degradation histories. To overcome these limitations, this investigation introduces a normalized crushing–critical state interaction parameter ϑ and a nonlinear tuning index δ into the UH-L model (Yao et al., 2021), leading to the development of the N-UH-LE model. This modified model provides a more comprehensive and accurate description of the stress–strain behavior of penetrated SMCGSs.

3.1. Normal consolidation line (NCL)

According to Yao and Fang (2020) and Chen et al. (2025), it is assumed that the NCL of SMCGS treated by penetrating erosion can be described by Eq. (11), detailed as Fig. 10:

$$e = Z - \lambda \ln\left(\frac{p + p_s}{1 + p_s}\right) \tag{11}$$

where Z represents the void ratio on the NCL at $p = 1$ kPa; λ refers to the slope of the NCL in the e-ln[$(p + p_s)/\vartheta$] space; p_s denotes the compression hardening parameter, as determined by

$$p_s = \exp\left(\frac{N - Z}{\lambda}\right) - 1 \tag{12}$$

where N refers to the void ratio on the NCL asymptote when $p = 1$ kPa in the e-ln(p/ϑ) space.

Based on Eq. (11), when the average stress increases from the initial average effective stress p_{x0} to p_x on the NCL, the total volume strain is

$$\varepsilon_v = \frac{\lambda}{1 + e_0} \ln\left(\frac{p_x + p_s}{p_{x0} + p_s}\right) \tag{13}$$

The elastic volume strain is

$$\varepsilon_v^e = \frac{\kappa}{1 + e_0} \ln\left(\frac{p_x + p_s}{p_{x0} + p_s}\right) \tag{14}$$

The plastic volume strain is

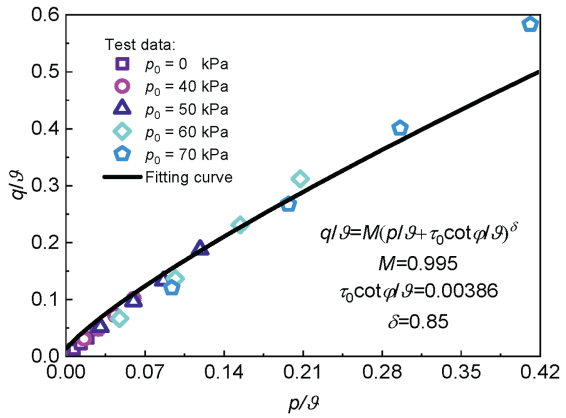

Fig. 9. CSL characterization on the p/ϑ - q/ϑ plane.

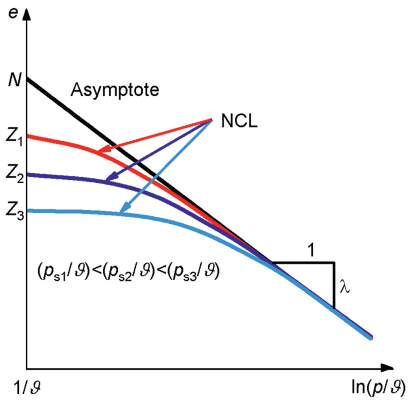

Fig. 10. Prediction of NCLs of SMCGS in the e-ln(p/ϑ) plane.

$$\varepsilon_v^p = \frac{\lambda-\kappa}{1+e_0}\ln\left(\frac{p_x+p_s}{p_{x0}+p_s}\right) \tag{15}$$

where κ refers to the expansion index of the e-ln(p/ϑ+p_s) space. p_x can be expressed as

$$p_x = p_{x0} + p_s \exp\left(\frac{\varepsilon_v^p}{c_p}\right) - p_s \tag{16}$$

where c_p=(λ-κ)/(1+e_0).

3.2. Shear behavior and description

A modified drop-shaped yield surface is utilized to describe the shear displacement in the N-UH-LE model (Yao et al., 2021). The equivalent normalized parameter ϑ relating particle crushing B_r* to plastic work W_p, along with the fine-tuning index δ for the nonlinear behavior of the CSL, is embedded in the yield function, enabling the characterization of penetrating erosion degradation and the nonlinear feature of the CSL (see Fig. 11 and Eqs. (17) and (18)):

$$f(\tilde{p},\tilde{q}) = 1 + \frac{(1+\chi)\tilde{\eta}^2}{M^2-\tilde{\eta}^2} - \frac{\tilde{p}_x}{\tilde{p}} = 0 \tag{17}$$

where

$$\left.\begin{aligned} \tilde{p} &= \left(\frac{p+\tau_0\cot\phi}{\vartheta}\right)^{\delta} \\ \tilde{q} &= q/\vartheta \\ \tilde{\eta} &= \frac{\tilde{q}}{\tilde{p}} \\ \tilde{p}_x &= \left(\frac{p_x+\tau_0\cot\phi}{\vartheta}\right)^{\delta} \end{aligned}\right\} \tag{18}$$

By integrating Eqs. (13) and (14), the initial yield function along the NCL is established as

$$f(\tilde{p},\tilde{q}) = \ln\left(1+\frac{(1+\chi)\tilde{\eta}^2}{M^2-\chi\tilde{\eta}^2}+\frac{p_s-\tau_0\cot\phi}{\vartheta\tilde{p}}\right) - \ln\left(\frac{p_{x0}-p_s}{\vartheta\tilde{p}}\right) - \frac{\varepsilon_v^p}{c_p} = 0 \tag{19}$$

The hardening parameter $d\varepsilon_v^p$ in Eq. (19) can be substituted with a unified hardening parameter H (detailed as Eq. (21)), enabling the yield function of the SMCGS corroded by penetration to be expressed as

$$f(\tilde{p},\tilde{q}) = \ln\left(1+\frac{(1+\chi)\tilde{\eta}^2}{M^2-\chi\tilde{\eta}^2}+\frac{p_s-\tau_0\cot\varphi}{\vartheta\tilde{p}}\right) - \ln\left(\frac{p_{x0}-p_s}{\vartheta\tilde{p}}\right) - \frac{H}{c_p} = 0 \tag{20}$$

$$H = \int dH = \int \frac{M_f^4-\tilde{\eta}^4}{M_c^4-\tilde{\eta}^4} d\varepsilon_v^p \tag{21}$$

where M_c represents the characteristic state stress ratio, with its calculation detailed in Section 2.3 below; M_f is defined as follows:

$$M_f = 6\left[\sqrt{\frac{k}{R}\left(1+\frac{k}{R}\right)} - \frac{k}{R}\right] \tag{22}$$

among which

$$k = \frac{M^2}{12(3-M)} \tag{23}$$

$$R = \exp\left(-\frac{\xi}{\lambda-\kappa}\right) \tag{24}$$

where ξ is defined as the state variable utilized to quantify the current density state of SMCGSs. As illustrated in Fig. 12, ξ corresponds to the vertical distance from the current density state A to the reference state E on the ACL (Adaptive Critical Line, which is employed to characterize the behavior and deformation properties of materials under various stress states), and can be obtained according to Eq. (25).

$$\xi = e_{\tilde{\eta}} - e \tag{25}$$

where e refers to the void ratio of the current state of SMCGS; $e_{\tilde{\eta}}$ denotes the void ratio on the ACL at the same mean effective stress and it can be expressed as

$$e_{\tilde{\eta}} = Z - \lambda\ln\left(\frac{p+p_s}{1+p_s}\right) - (\lambda-\kappa)\ln\left(1+\frac{\vartheta\tilde{p}(1+\chi)\tilde{\eta}^2}{(p+p_s)\left(M^2-\chi\tilde{\eta}^2\right)}\right) \tag{26}$$

when $e_{\tilde{\eta}} = M$, the CSL can be derived as

$$e_{\tilde{\eta}} = Z - \lambda\ln\left(\frac{p+p_s}{1+p_s}\right) - (\lambda-\kappa)\ln\left(1+\frac{\vartheta\tilde{p}(1+\chi)}{(p+p_s)(1-\chi)}\right) \tag{27}$$

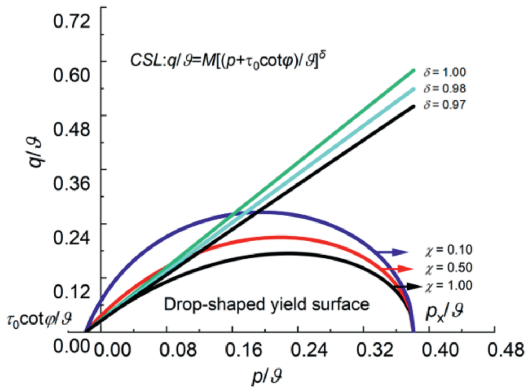

Fig. 11. Drop-shaped yield surface considering nonlinear CSL in the p/ϑ - q/ϑ plane.

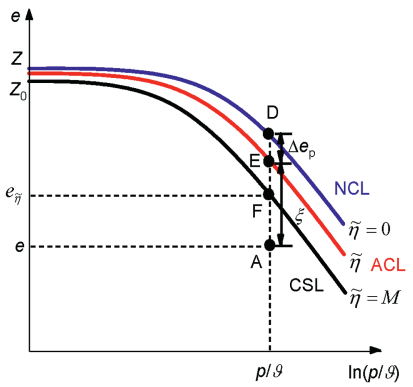

Fig. 12. NCL and ACL in the e-ln(p/ϑ) plane and state variable ξ.

3.3. Dilation equation and plastic potential function

The nonlinear morphological fine-tuning index (δ) of the CSL in the p/ϑ - q/ϑ plane is incorporated into the dilatancy equation of the UH-L model (Yao and Fang, 2020), and the dilatancy equation of the N-UH-LE model for SMCGS, accounting for the effects of penetrating erosion, is formulated as follows.

$$\frac{\mathrm{d}\varepsilon_{\mathrm{v}}^{\mathrm{p}}}{\mathrm{d}\varepsilon_{\mathrm{d}}^{\mathrm{p}}}=\frac{M_{\mathrm{c}}^2-\tilde{\eta}^2}{2\tilde{\eta}} \tag{28}$$

where M_{c} ia able to be demonstrated as

$$M_{\mathrm{c}}=M\exp(-m\xi) \tag{29}$$

where m denotes a parameter governing the evolution of M_{c} with respect to the state variable ξ. Based on Eq. (28), the plastic potential function can be expressed as follows:

$$g(\tilde{p},\tilde{q})=1+\frac{\tilde{\eta}^2}{M_{\mathrm{c}}^2}-\frac{\tilde{p}_x}{\tilde{p}}=0 \tag{30}$$

A comparison between Eq. (30) and Eq. (17) indicates that the N-UH-LE model employs a non-associated flow rule.

3.4. Strain increment

3.4.1. Elastic strain increment

Determine the elastic strain increment in accordance with Hooke's law (see Eq. (31)).

$$\left.\begin{aligned}\mathrm{d}\varepsilon_{\mathrm{v}}^{\mathrm{e}}&=\frac{\mathrm{d}p}{K}\\ \mathrm{d}\varepsilon_{\mathrm{d}}^{\mathrm{e}}&=\frac{\mathrm{d}q}{3G}\end{aligned}\right\} \tag{31}$$

where K and G refer to the bulk modulus and shear modulus, respectively, which are obtained from Eqs. (32)–(34).

$$K=\frac{E}{3(1-2\nu)} \tag{32}$$

$$G=\frac{E}{2(1+2\nu)} \tag{33}$$

$$E=\frac{3(1-2\nu)(1+e_0)}{\kappa}\cdot\left(p+\vartheta\cdot\frac{p_{\mathrm{s}}}{\vartheta}\right) \tag{34}$$

among which, ν refers to Poisson's ratio; E denotes the elastic modulus.

3.4.2. Plastic strain increment

The plastic strain increment is able to be computed using the non-associative flow law.

$$\left.\begin{aligned}\mathrm{d}\varepsilon_{\mathrm{v}}^{\mathrm{p}}&=\Lambda\frac{\partial g(\tilde{p},\tilde{q})}{\partial p}\\ \mathrm{d}\varepsilon_{\mathrm{d}}^{\mathrm{p}}&=\Lambda\frac{\partial g(\tilde{p},\tilde{q})}{\partial q}\end{aligned}\right\} \tag{35}$$

The plasticity factor Λ in Eq. (35) can be derived as follows. Specifically, applying the total differential of Eq. (20) leads to Eq. (36).

$$\mathrm{d}f(\tilde{p},\tilde{q})=\frac{\partial f(\tilde{p},\tilde{q})}{\partial p}\mathrm{d}p+\frac{\partial f(\tilde{p},\tilde{q})}{\partial q}\mathrm{d}q+\frac{\partial f(\tilde{p},\tilde{q})}{\partial H}\frac{\partial H}{\partial\varepsilon_{\mathrm{v}}^{\mathrm{p}}}\mathrm{d}\varepsilon_{\mathrm{v}}^{\mathrm{p}}=0 \tag{36}$$

By simultaneously considering Eqs. (20), (21), (35) and (36), the following results can be obtained.

$$\frac{\partial f(\tilde{p},\tilde{q})}{\partial p}\mathrm{d}p+\frac{\partial f(\tilde{p},\tilde{q})}{\partial q}\mathrm{d}q-\frac{1}{c_{\mathrm{p}}}\frac{M_{\mathrm{f}}^4-\tilde{\eta}^4}{M_{\mathrm{c}}^4-\tilde{\eta}^4}\Lambda\frac{\partial g(\tilde{p},\tilde{q})}{\partial p}=0 \tag{37}$$

Then, the plasticity factor Λ can thus be determined.

$$\Lambda=c_{\mathrm{p}}\Omega\frac{\frac{\partial f(\tilde{p},\tilde{q})}{\partial p}\mathrm{d}p+\frac{\partial f(\tilde{p},\tilde{q})}{\partial q}\mathrm{d}q}{\frac{\partial g(\tilde{p},\tilde{q})}{\partial p}} \tag{38}$$

where

$$\Omega=\frac{M_{\mathrm{c}}^4-\tilde{\eta}^4}{M_{\mathrm{f}}^4-\tilde{\eta}^4} \tag{39}$$

In accordance with the chain rule, it can be stated that

$$\frac{\partial f(\tilde{p},\tilde{q})}{\partial p}=\frac{\partial f(\tilde{p},\tilde{q})}{\partial\tilde{p}}\frac{\partial\tilde{p}}{\partial p}=\frac{\partial f(\tilde{p},\tilde{q})}{\partial\tilde{p}}\cdot\frac{\delta}{\vartheta}\left(\frac{p+\tau_0\cot\varphi}{\vartheta}\right)^{\delta-1} \tag{40}$$

$$\frac{\partial f(\tilde{p},\tilde{q})}{\partial q}=\frac{\partial f(\tilde{p},\tilde{q})}{\partial\tilde{q}}\frac{\partial\tilde{q}}{\partial q}=\frac{\partial f(\tilde{p},\tilde{q})}{\partial\tilde{q}}\cdot\frac{1}{\vartheta} \tag{41}$$

$$\frac{\partial g(\tilde{p},\tilde{q})}{\partial p}=\frac{\partial g(\tilde{p},\tilde{q})}{\partial\tilde{p}}\frac{\partial\tilde{p}}{\partial p}=\frac{\partial g(\tilde{p},\tilde{q})}{\partial\tilde{p}}\cdot\frac{\delta}{\vartheta}\left(\frac{p+\tau_0\cot\varphi}{\vartheta}\right)^{\delta-1} \tag{42}$$

$$\frac{\partial g(\tilde{p},\tilde{q})}{\partial q}=\frac{\partial g(\tilde{p},\tilde{q})}{\partial\tilde{q}}\frac{\partial\tilde{q}}{\partial q}=\frac{\partial g(\tilde{p},\tilde{q})}{\partial\tilde{q}}\cdot\frac{1}{\vartheta} \tag{43}$$

Combined with (Yao and Fang, 2020), then

$$\left.\begin{aligned}\frac{\partial f(\tilde{p},\tilde{q})}{\partial p}&=\frac{M^4-(1+3\chi)M^2\tilde{\eta}^2-\chi\tilde{\eta}^4}{\tilde{p}\left(M^2-\chi\tilde{\eta}^2\right)\left[M^2+\tilde{\eta}^2+\left(M^2-\chi\tilde{\eta}^2\right)(p_{\mathrm{s}}-\tau_0\cot\phi)\big/\tilde{p}\right]}\cdot\frac{\delta}{\vartheta}\left(\frac{p+\tau_0\cot\phi}{\vartheta}\right)^{\delta-1}\\ \frac{\partial f(\tilde{p},\tilde{q})}{\partial q}&=\frac{2M^2(1+\chi)\tilde{\eta}}{\tilde{p}\left(M^2-\chi\tilde{\eta}^2\right)\left[M^2+\tilde{\eta}^2+\left(M^2-\chi\tilde{\eta}^2\right)(p_{\mathrm{s}}-\tau_0\cot\phi)\big/\tilde{p}\right]}\cdot\frac{1}{\vartheta}\end{aligned}\right\} \tag{44}$$

$$\left.\begin{aligned}\frac{\partial g(\tilde{p},\tilde{q})}{\partial p}&=\frac{M_{\mathrm{c}}^2-\tilde{\eta}^2}{\tilde{p}\left(M_{\mathrm{c}}^2+\tilde{\eta}^2\right)}\cdot\frac{\delta}{\vartheta}\left(\frac{p+\tau_0\cot\phi}{\vartheta}\right)^{\delta-1}\\ \frac{\partial g(\tilde{p},\tilde{q})}{\partial q}&=\frac{2\tilde{\eta}}{\tilde{p}\left(M_{\mathrm{c}}^2+\tilde{\eta}^2\right)}\cdot\frac{1}{\vartheta}\end{aligned}\right\} \tag{45}$$

3.5. Elasto-plastic stress and strain in the p - q plane

The total volumetric strain increment $d\varepsilon_v$ can be regarded as the sum of the elastic $d\varepsilon_v^e$ and plastic $d\varepsilon_v^p$ volumetric strain increments, while the total shear strain increment can be viewed as the sum of the elastic $d\varepsilon_d^e$ and plastic $d\varepsilon_d^p$ shear strain increments, as detailed in Eq. (46). The superposition of these strain increments reflects the overall strain response of SMCGS subjected to external loading.

$$\left.\begin{aligned} d\varepsilon_v &= d\varepsilon_v^e + d\varepsilon_v^p \\ d\varepsilon_d &= d\varepsilon_d^e + d\varepsilon_d^p \end{aligned}\right\} \tag{46}$$

By combining Eqs. ((31), (35), (38) and (39), the stress-strain relationship of the N-UH-LE model in the p - q plane can be derived, as demonstrated in Eq. (47):

$$\begin{Bmatrix} d\varepsilon_v \\ d\varepsilon_d \end{Bmatrix} = \begin{bmatrix} \dfrac{1}{K}+\Omega\dfrac{\partial f(\tilde{p},\tilde{q})}{\partial p} & \Omega\dfrac{\partial f(\tilde{p},\tilde{q})}{\partial q} \\ \Omega\dfrac{\partial g(\tilde{p},\tilde{q})/\partial q}{\partial g(\tilde{p},\tilde{q})/\partial p}\dfrac{\partial f(\tilde{p},\tilde{q})}{\partial p} & \dfrac{1}{3G}+\Omega\dfrac{\partial g(\tilde{p},\tilde{q})/\partial q}{\partial g(\tilde{p},\tilde{q})/\partial p}\dfrac{\partial f(\tilde{p},\tilde{q})}{\partial q} \end{bmatrix} \begin{Bmatrix} dp \\ dq \end{Bmatrix} \tag{47}$$

The stress-strain relationship presented in Eq. (47) can be expressed as

$$\begin{Bmatrix} d\varepsilon_v \\ d\varepsilon_d \end{Bmatrix} = \begin{bmatrix} C_{11} & C_{12} \\ C_{21} & C_{22} \end{bmatrix} \begin{Bmatrix} dp \\ dq \end{Bmatrix} \tag{48}$$

By simultaneously considering Eqs. (44) and (45), the coefficients C_{11}, C_{12}, C_{21}, and C_{22} in Eq. (48) can be determined as

$$\left.\begin{aligned} C_{11} &= \frac{1}{K}+\frac{M_c^4-\tilde{\eta}^4}{M_f^4-\tilde{\eta}^4}\frac{M^4-(1+3\chi)M^2\tilde{\eta}^2-\chi\tilde{\eta}^4}{\tilde{p}\left(M^2-\chi\tilde{\eta}^2\right)\left[M^2+\tilde{\eta}^2+\left(M^2-\chi\tilde{\eta}^2\right)(p_s-\tau_0\cot\phi)/\tilde{p}\right]}\cdot\frac{\delta}{\vartheta}\left(\frac{p+\tau_0\cot\phi}{\vartheta}\right)^{\delta-1} \\ C_{12} &= \frac{M_c^4-\tilde{\eta}^4}{M_f^4-\tilde{\eta}^4}\frac{2M^2(1+\chi)\tilde{\eta}}{\tilde{p}\left(M^2-\chi\tilde{\eta}^2\right)\left[M^2+\tilde{\eta}^2+\left(M^2-\chi\tilde{\eta}^2\right)(p_s-\tau_0\cot\phi)/\tilde{p}\right]}\cdot\frac{1}{\vartheta} \\ C_{21} &= \frac{M_c^4-\tilde{\eta}^4}{M_f^4-\tilde{\eta}^4}\frac{2\tilde{\eta}}{M_c^2-\tilde{\eta}^2}\frac{M^4-(1+3\chi)M^2\tilde{\eta}^2-\chi\tilde{\eta}^4}{\tilde{p}\left(M^2-\chi\tilde{\eta}^2\right)\left[M^2+\tilde{\eta}^2+\left(M^2-\chi\tilde{\eta}^2\right)(p_s-\tau_0\cot\phi)/\tilde{p}\right]}\cdot\frac{1}{\vartheta} \\ C_{22} &= \frac{1}{3G}+\frac{M_c^4-\tilde{\eta}^4}{M_f^4-\tilde{\eta}^4}\frac{2\tilde{\eta}}{M_c^2-\tilde{\eta}^2}\frac{2M^2(1+\chi)\tilde{\eta}}{\tilde{p}\left(M^2-\chi\tilde{\eta}^2\right)\left[M^2+\tilde{\eta}^2+\left(M^2-\chi\tilde{\eta}^2\right)(p_s-\tau_0\cot\phi)/\tilde{p}\right]}\cdot\frac{1}{\vartheta\delta}\left(\frac{\vartheta}{p+\tau_0\cot\phi}\right)^{\delta-1} \end{aligned}\right\} \tag{49}$$

4. Parameter calibration

The parameter calibration for the N-UH-LE constitutive model is explained through taking Chen et al. (2025) as a case study.

4.1. Normalized parameter (ϑ)

According to Chen et al. (2025), the relationships between B_r* and W_p subject to various settings of p_0 are illustrated in Fig. 13. The parameters α and n can be obtained through fitting the above relationships based on Eq. (4). Subsequently, the normalization parameter ϑ under different settings is determined in accordance with Eq. (5), detailed as Table 3. After normalization, the statistical properties of particle crushing on the B_r*-W_p/ϑ plane are demonstrated in Fig. 14.

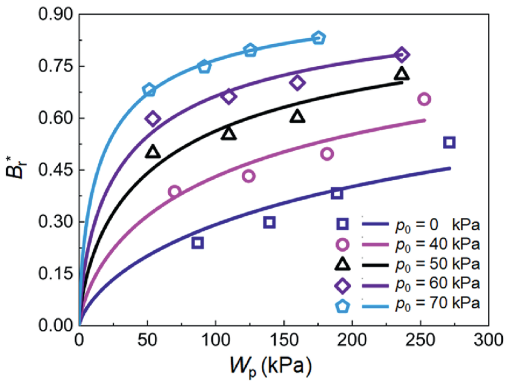

Fig. 13. Relationship between B_r* and W_p subject to various settings of p_0.

Table 3
Normalized parameters ϑ subject to different conditions of p_0.

Parameter	Penetration erosion intensity, p_0 (kPa)				
	0	40	50	60	70
ϑ	35056.18	14797.57	6993.09	3823.85	1832.80

4.2. State parameters (λ, κ, and ν)

The compression index λ and rebound index κ of SMCGS are calibrated based on the one-dimensional consolidation compression test. The compression outcome of the SMCGS specimen without penetrating erosion is presented in Fig. 15. The slopes (λ, κ) of the asymptotes of the e-ln$p$ curve during the compression phase (NCL) and rebound phase are 0.0904 and 0.063, respectively.

The Poisson's ratio ν of the SMCGS specimen was calibrated anchored in the correlation between shear strain ε_d and volumetric strain ε_v, as described in Eq. (50). The converted Poisson's ratios ν for both untreated SMCGS specimens and those treated with varying penetration erosion intensities subjected to various confining pressures σ_3 are demonstrated in Fig. 16. The Poisson's ratio ν for SMCGS specimens can be determined to be 0.407.

$$\nu = \frac{\varepsilon_d - \varepsilon_v}{2\varepsilon_d + \varepsilon_v} \tag{50}$$

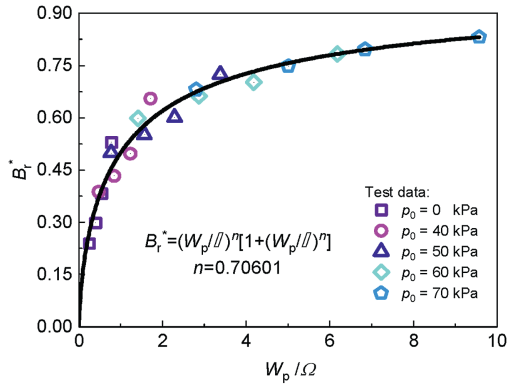

Fig. 14. The statistical properties of particle breakage on the B_r*-W_p/ϑ plane.

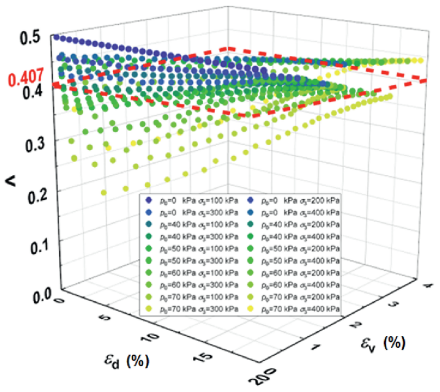

Fig. 16. The converted Poisson's ratios ν for SMCGS specimens under various σ_3.

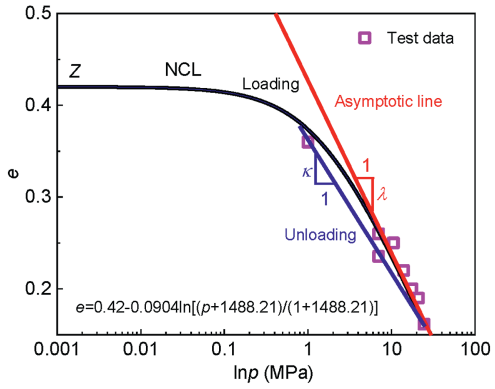

Fig. 15. The NCL of SMCGS specimen in the e-ln$p$ space.

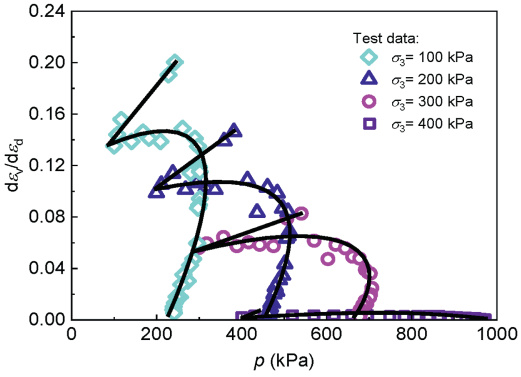

Fig. 17. The $d\varepsilon_v/d\varepsilon_d$ - p relationships for SMCGS specimens without penetrating erosion.

4.3. Nonlinear and hardening parameters ($\tau_0 \cot\varphi$, δ, M, and N)

As illustrated in Fig. 9, the normalized particle interlocking stress $\tau_0 \cot\varphi/\vartheta$, the nonlinear fine-tuning index δ of the CSL, and the slope M of the CSL in the p/ϑ - q/ϑ plane are calibrated to be 0.00386, 0.85, and 0.995, respectively. As for critical state parameter N, it is defined as the void ratio on the NCL asymptote when $p = 1$ kPa in the e-ln$p$ plane. As depicted in Fig. 15, in the absence of penetration erosion treatment (i.e. $p_0 = 0$ kPa and $\vartheta = 35056.18$), the value of N can be determined to be 1.084.

4.4. Unified hardening parameter (Z and p_s)

According to Eq. (10), the NCL of the untreated SMCGS specimen in Fig. 15 was derived, and the unified hardening parameters Z and p_{s1}, subjected to the setting of $p_0 = 0$ kPa and $\vartheta = 35056.18$, were estimated to be 0.42 and 1488.21 kPa. Simultaneously, the value of p_{s1} obtained through inversion through Eq. (10) is determined to be 1547.64 kPa, differing by 59.43 kPa from that derived using Eq. (9). The relative error is only 3.99 %, indicating that the obtained p_{s1} can be reliable. Upon normalization, the p_s/ϑ can be found to be 0.04245.

4.5. Evolution parameters (χ and m)

4.5.1. Critical state parameter (χ)

In the N-UH-LE model, the critical state parameter χ not only alters the shape of the yield surface but also adjusts the vertical distance between the NCL and CSL. As depicted in Fig. 12, when $p/\vartheta > 0$ kPa, the vertical distance $\Delta\bar{e}_p$ between the NCL and CSL is influenced by the critical state parameter χ. Therefore, parameter χ regulates the vertical separation between the NCL and CSL for $p/\vartheta > 0$ kPa. The expression for parameter χ can be derived from Eq. (51) as follows.

$$\chi = 1 - \frac{2\cdot\frac{p}{\vartheta}}{\left(\frac{p}{\vartheta}+\frac{p_s}{\vartheta}\right)\exp\left(\frac{\Delta\bar{e}_p}{\lambda-\kappa}\right)-\frac{p_s}{\vartheta}} \tag{51}$$

It is evident that if the vertical distance $\Delta\bar{e}_p$ between the NCL and CSL at a known normalized stress p/ϑ can be measured based on the test results, the parameter χ can be calculated by substituting the known normalized stress p/ϑ and the measured $\Delta\bar{e}_p$ into Eq. (51). Then, the χ can be concluded through inserting the above determined values $\Delta\bar{e}_p$, λ, κ, and p_s/ϑ into Eq. (51)., detailed as 0.29.

4.5.2. Dilatancy parameter (m)

The dilatancy parameter m significantly affects the changes of the characteristic stress ratio M_c with respect to state parameter ξ_c. The characteristic state refers to the condition at which contraction transitions to dilation, i.e. when the increment of plastic volumetric strain equals zero ($d\varepsilon_v = 0$). To this end, the $d\varepsilon_v/d\varepsilon_d$ - p relationships were analyzed for SMCGS specimens without penetrating erosion under various confining pressures σ_3, detailed in Fig. 17. Then, the mean normal stresses p_{ξ_c} and stress ratios $M_c^{\xi_c}$ at $d\varepsilon_v = 0$ can be identified, subjected to the four confining pressures. Thereafter, the void ratio $e_{\tilde{\eta}}$ at the characteristic stress state

Table 4
The calibrated parameters of N-UH-LE constitutive model for SMCGS.

p_0 (kPa)	Normalized parameter	State parameter			Nonlinear parameter			Hardening parameter		Unified hardening parameter			Evolution parameter	
	ϑ	λ	κ	ν	$\tau_0\cot\varphi$ (kPa)	$\tau_0\cot\varphi/\vartheta$	δ	M	N	Z	p_s (kPa)	(p_s/ϑ) (kPa)	χ	m
0	35056.18	0.0904	0.063	0.41	135.32	0.00386	0.85	0.995	1.084	0.39–0.42	1488.21	0.042–0.329	0.29	0.1
40	14797.57				57.12						1350.31			
50	6993.09				26.99						1100.64			
60	3823.85				14.76						947.12			
70	1832.80				7.07						602.45			

could be obtained by substituting the p_{ξ_c} and $M_c^{\xi_c}$ into Eq. (26). Subsequently, the ξ_c corresponding to the $M_c^{\xi_c}$ can be acquired based on Eq. (25). Finally, it is found that $m = 0.1$ after averaging through plugging $M_c^{\xi_c}$ and ξ_c into Eq. (29) in this case study.

$$m = -\frac{1}{\xi_c}\ln\left(\frac{M_c^{\xi_c}}{M}\right) \tag{52}$$

Integrating Sections 4.1 to 4.5, the calibrated N-UH-LE constitutive model parameters for the case study in this investigation are illustrated in Table 4.

5. Model validation

To present the reliability of the N-UH-LE model, the properties of the N-UH-LE model are verified with the CD triaxial compression tests (Chen et al., 2025). The parameters utilized in the model are demonstrated in Table 3 (the normalized parameter is

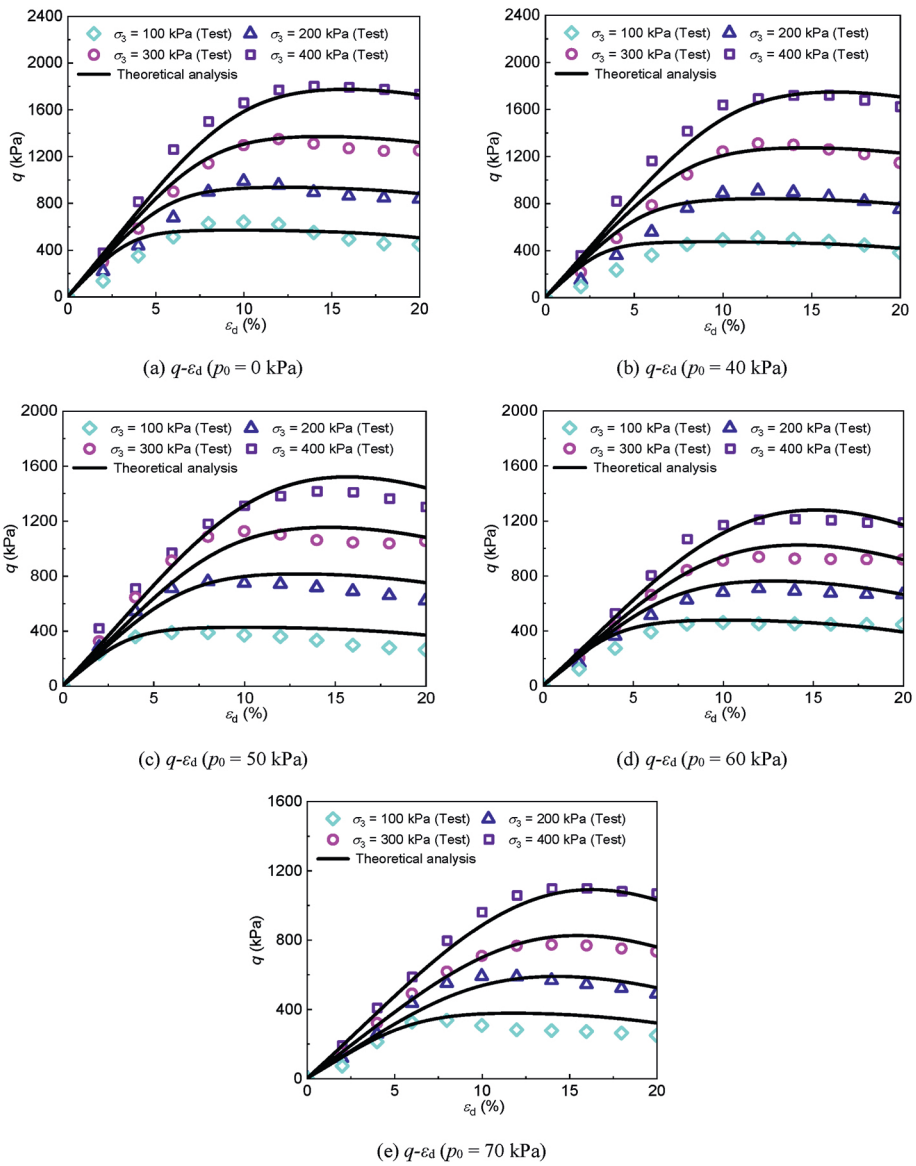

(a) q-ε_d ($p_0 = 0$ kPa) (b) q-ε_d ($p_0 = 40$ kPa)

(c) q-ε_d ($p_0 = 50$ kPa) (d) q-ε_d ($p_0 = 60$ kPa)

(e) q-ε_d ($p_0 = 70$ kPa)

Fig. 18. Comparison of the prediction of N-UH-LE model with experimental CD triaxial data for SMCGS specimen subjected to various penetrating erosion intensities.

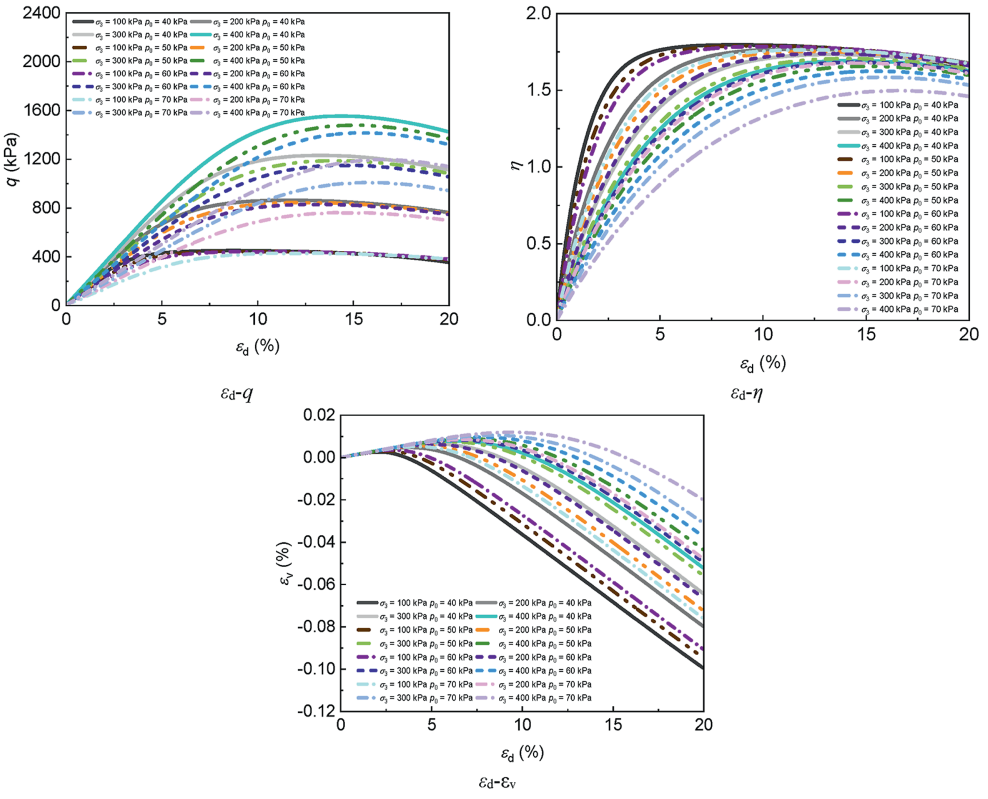

(a) $e_0 = 0.3$

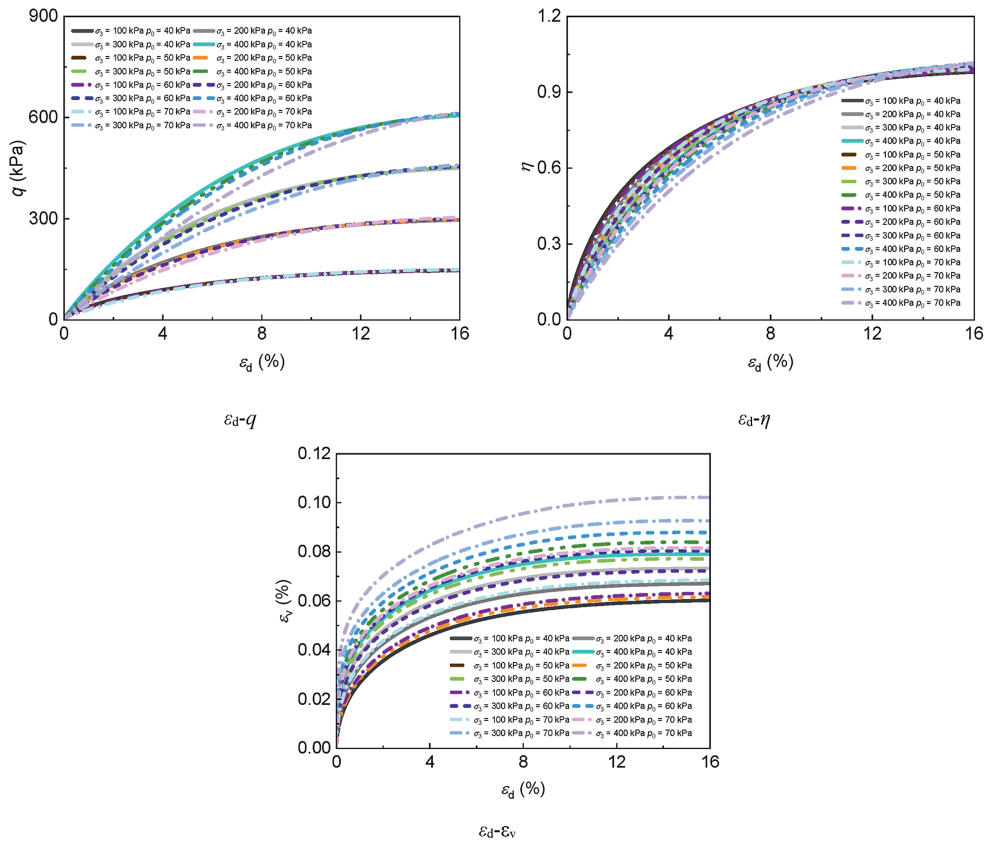

(b) $e_0 = 0.5$

Fig. 19. Influence of initial void ratio e_0 on shearing of SMCGS subjected to penetration erosion.

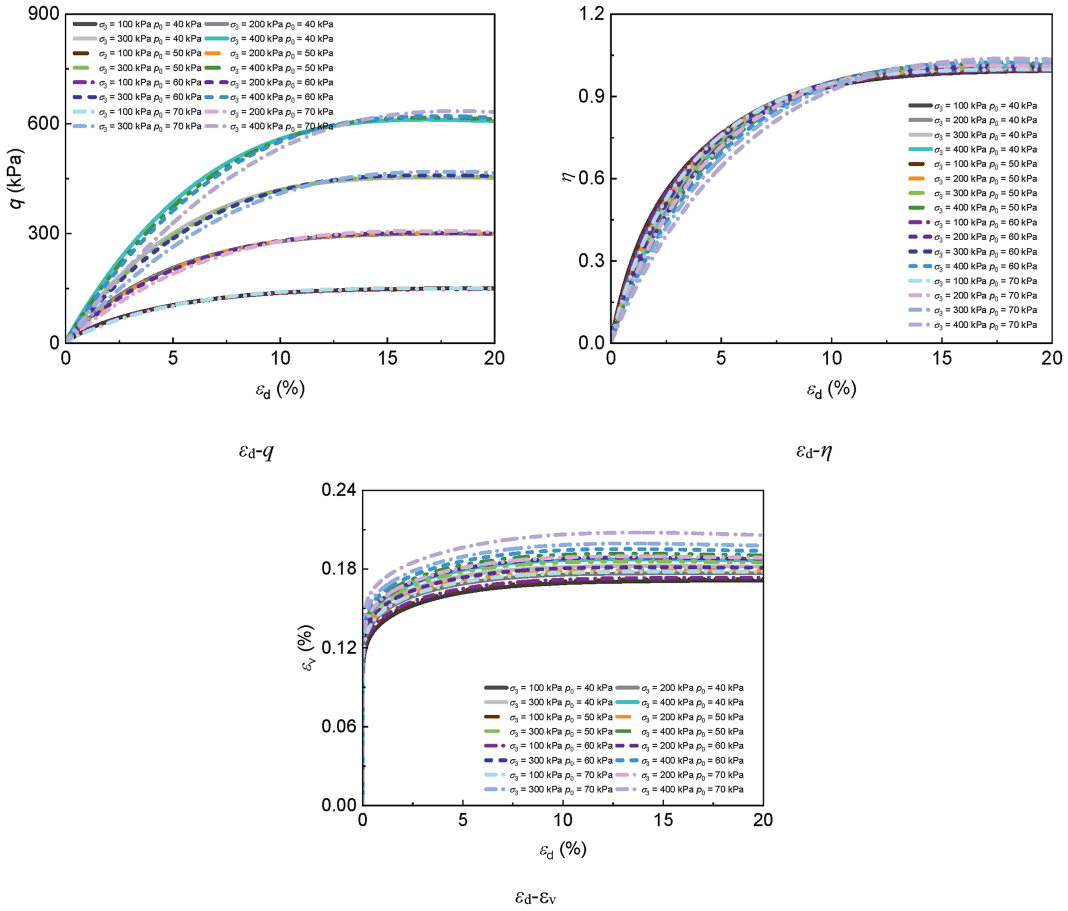

(c) $e_0 = 0.7$

Fig. 19. (*continued*).

formulated anchored in an improved relative breakage potential (B_r*), and certain errors are unavoidable in the B_r* obtained via vibrating screening, given the limited frequency of parallel tests. Consequently, the unified hardening parameters z and p_s, derived through normalized parameter conversions, may deviate from reality. Thus, the adaptive adjustments are implemented for z and p_s to improve accuracy, as detailed in Table 3. The verification outcomes are detailed in Fig. 18. Triaxial experiments carried out under confining stresses of 100–400 kPa enabled a comparison between model-derived deviatoric stress–shear strain curves and test measurements, yielding a maximum relative error below 7.76 % and demonstrating excellent concordance, notably in the terminal loading phases. Concurrently, the N-UH-LE model's capacity to reliably reflect both hardening and softening responses across varied loading scenarios was confirmed.

6. Discussion

6.1. Influence of initial void ratio (e_0)

The SMCGSs with a higher initial void ratio e_0 are more prone to particle migration and reconstitution during penetrating erosion, changing the pore structure and a subsequent reduction in strength, and then exacerbating the erosion. Consequently, the initial void ratio e_0 is a critical factor influencing the resistance of SMCGS to penetrating erosion. Three initial void ratios (e_0) of 0.3, 0.5, and 0.7 were set to explore the mechanical features of SMCGS specimens subjected to varying penetrating erosion conditions.

As demonstrated in Fig. 19, the modified N-UH-LE model in this study effectively characterizes the strain hardening, softening, and dilation behaviors of coarse-grained soils. Specifically, when the initial void ratio is low ($e_0 = 0.3$), SMCGS exhibits initial hardening followed by softening, along with pronounced dilation. Conversely, at higher initial void ratios ($e_0 = 0.5$ or 0.7), SMCGS demonstrates distinct loading hardening and contraction behavior. At a low initial void ratio ($e_0 = 0.3$), SMCGS exhibits considerable variability in performance degradation due to penetrating erosion, and the variability is reduced as confining pressure σ_3 decreases and initial void ratio increases e_0. This phenomenon can be attributed to the similarity in loading paths observed in the specimens subjected to low confining pressure of triaxial testing, which may result in consistent stress states and deformation behavior, thereby reducing variability in performance due to seepage erosion. Furthermore, when the initial void ratio is relatively high ($e_0 = 0.5$ or 0.7), the interactions between particles are diminished, making it more challenging for penetrating flow to induce particle movement and structural damage, ultimately leading to relatively stable performance.

6.2. Effects of interlocking strength ($\tau_0 \cot\varphi$)

The particle interlocking effect, commonly quantified by interlocking strength $\tau_0 \cot\varphi$, minimizes the potential for relative particle displacement, thereby preserving soil compactness and

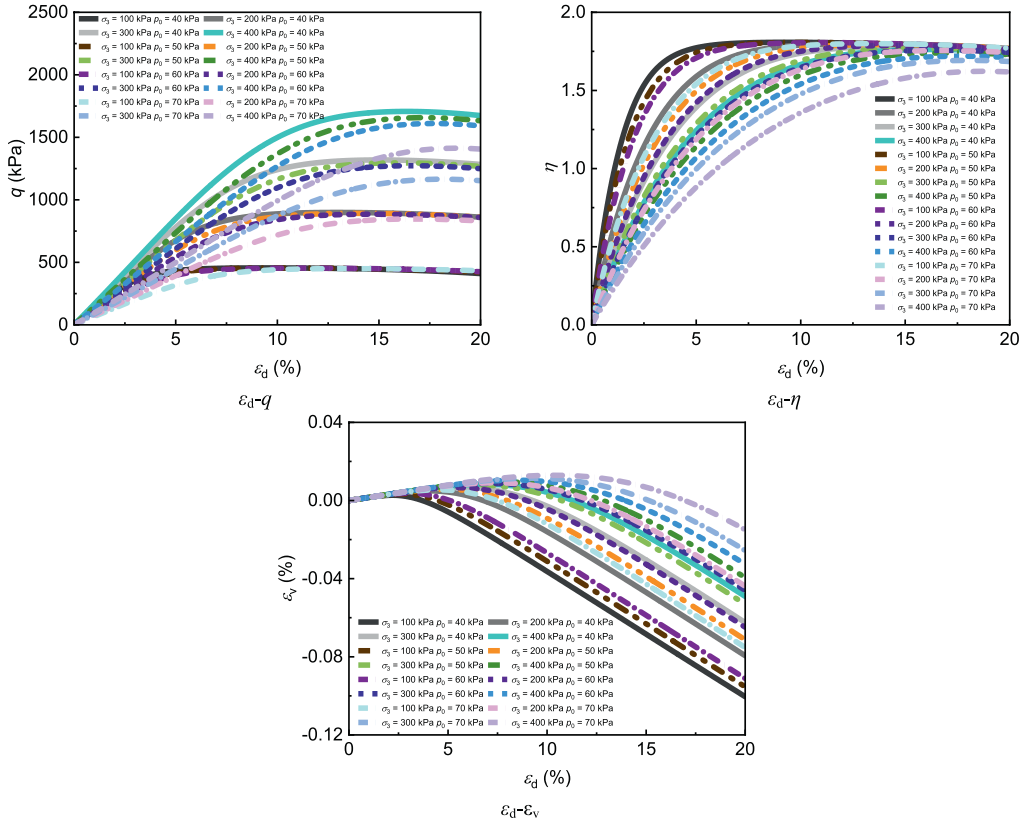

(a) $\tau_0 \cot\varphi = 40$ kPa

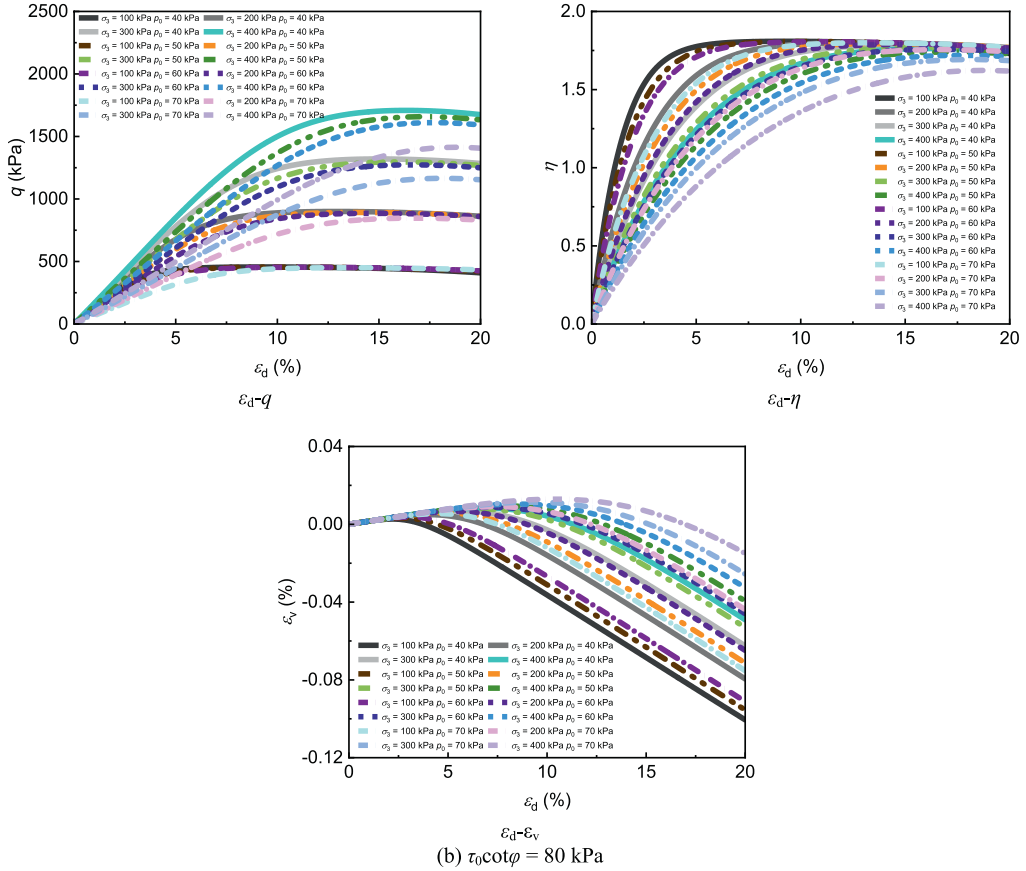

(b) $\tau_0 \cot\varphi = 80$ kPa

Fig. 20. Effects of interlocking strength $\tau_0 \cot\varphi$ on shearing of SMCGS subjected to penetration erosion.

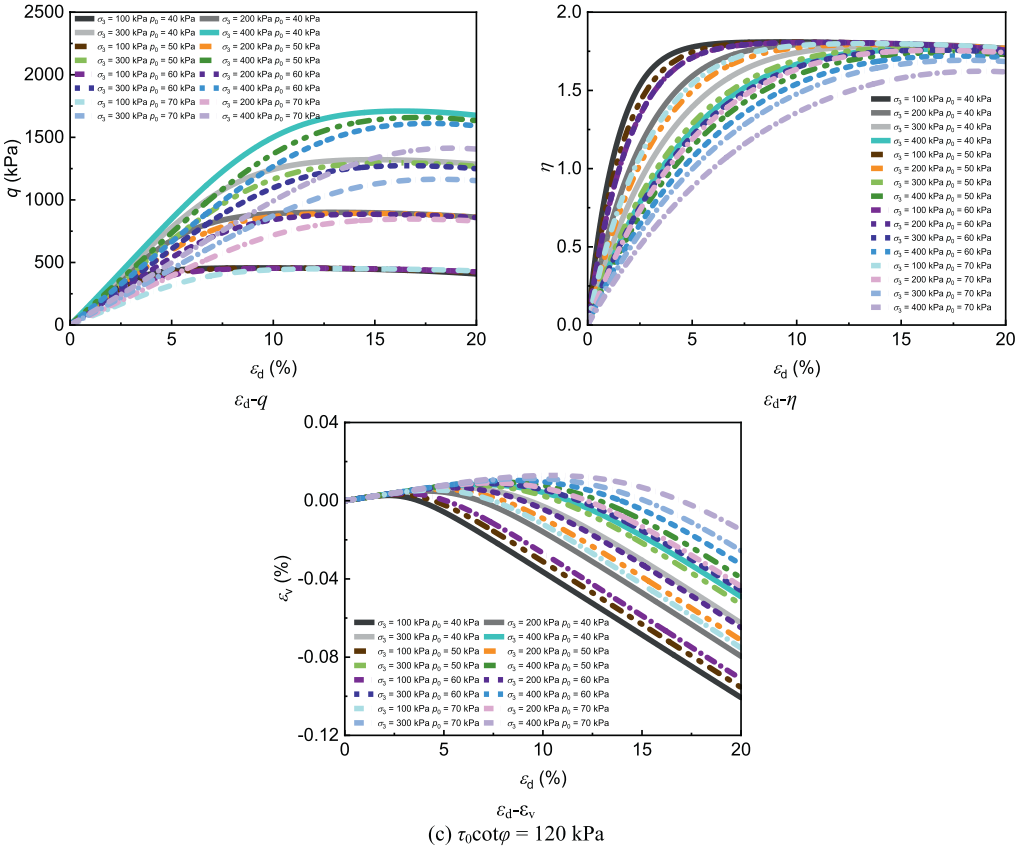

(c) $\tau_0 \cot\varphi$ = 120 kPa

Fig. 20. (*continued*).

internal structural integrity, which inhibits the fine particle migration caused by penetrating erosion, effectively mitigating the advancement of seepage erosion. To evaluate the penetrating erosion resistance as influenced by interlocking effects characterized by the N-UH-LE model, this section introduces three initial interlocking strengths $\tau_0 \cot\varphi$ of 40 kPa, 80 kPa, and 120 kPa were introduced to examine the mechanical behavior of SMCGS specimens under varying penetrating erosion conditions.

As illustrated in Fig. 20, when the initial void ratio remains constant, variations in interlocking strength (defined by the arrangement of particles) have negligible effects on the degradation differences induced by penetrating erosion. This phenomenon can be elucidated through the following considerations: (1) The initial void ratio determines the internal pore space and relative positioning of particles within the soil matrix. When the void ratio is held constant, the overall structural integrity and flow characteristics of the soil remain largely unchanged. Consequently, even if the arrangement of particles shifts, the response to penetrating water flow exhibits minimal variation. (2) Although interlocking strength affects particle interactions, its impact on the soil's overall resistance to penetrating erosion is limited when the initial void ratio is fixed. While interlocking may enhance the stability of the soil to some degree, other critical factors (e.g. flow velocity, particle morphology, and soil cohesion) often play a more dominant role during the process of penetrating erosion. (3) Penetrating erosion is inherently complex, influenced by a multitude of interrelated factors. Even with changes in interlocking strength, if other conditions remain unchanged, the effects on performance degradation due to penetrating erosion are likely to be diluted.

7. Conclusions

This study investigates the mechanical behavior of SMCGSs under penetrating erosion and proposes a modified constitutive model to capture erosion-induced degradation and critical state evolution at low confining pressures. Based on consolidated drained triaxial tests and theoretical developments, the main conclusions are summarized as follows:

(1) The N-UH-LE model, developed by incorporating a normalized parameter ϑ and a nonlinear tuning index δ into the unified hardening model under low confining pressure (UH-L), effectively characterizes the nonlinear mechanical behavior of brittle SMCGS at the critical state. It successfully reproduces key stress–strain features such as hardening, softening, and shear dilation under constant erosion conditions, while also capturing volumetric changes induced by varying erosion intensities.
(2) The model predictions of deviatoric stress–shear strain responses align closely with consolidated drained triaxial test data, with a maximum relative error of 7.76 %, validating the model's capability to simulate the mechanical properties of friable SMCGS subjected to penetrating erosion at low confining pressures.
(3) The extent of degradation induced by penetrating erosion decreases with lower confining pressure (σ_3) and higher initial void ratio (e_0), while changes in interlocking strength have a limited impact on degradation variability.

Despite its advantages, the N-UH-LE model has several limitations that warrant further improvement.

(1) The normalized parameter ϑ is formulated based on an improved relative breakage potential B_r*, and certain errors are unavoidable in the B_r* obtained via vibrating screening, given the limited frequency of parallel tests. Consequently, the unified hardening parameters z and p_s, derived through normalized parameter conversions, may deviate from reality.
(2) The calibration of N-UH-LE model parameters solely based on one-dimensional consolidation compression tests and normalized conversion derived from non-penetrated SMCGS specimens is relatively limited. It is necessary to further conduct one-dimensional consolidation compression tests on those subjected to various penetrating erosion intensities to validate the parameters obtained through normalized conversion.

From an engineering perspective, the N-UH-LE model can offer a useful tool for evaluating the mechanical performance and long-term stability of infrastructure such as embankments, subgrades, and backfills constructed with weak mudstone-derived coarse-grained materials in regions prone to internal erosion and rainfall infiltration. Its ability to capture both mechanical degradation and nonlinear critical state behavior under erosion makes it especially relevant for predicting deformation and failure in soft rock terrain.

Subsequent investigations should endeavor to enhance the robustness and applicability of the N-UH-LE model. One promising direction is broadening the model toward three-dimensional stress, thereby enabling simulation of more complex field loading scenarios. Additionally, incorporating cyclic loading effects would allow the model to simulate long-term performance under repeated traffic or seismic loads. Expanding the model's validation to include coarse-grained geomaterials derived from other rock types and subjected to diverse hydromechanical coupling processes (e.g. wetting–drying, chemical weathering) would further establish its generality. These efforts will contribute to developing a more comprehensive and reliable constitutive model for rock-derived coarse-grained soils in geotechnical applications.

CRediT authorship contribution statement

Ling Zhang: Funding acquisition, Writing – original draft, Supervision. **Yunhao Chen:** Funding acquisition, Data curation, Methodology, Formal analysis, Writing – original draft, Validation, Writing – review & editing. **Xuzhen He:** Writing – review & editing, Supervision, Writing – original draft. **Shaoheng Dai:** Visualization, Writing – review & editing, Writing – original draft. **Biao Luo:** Writing – review & editing, Writing – original draft. **Daichao Sheng:** Writing – review & editing.

Declaration of competing interest

The authors declare that they have no known competing financial interests or personal relationships that could have appeared to influence the work reported in this paper.

Acknowledgments

This study was supported by the National Natural Science Foundation of China (Grant No. 52378340), the Postgraduate Scientific Research Innovation Project of Hunan Province (Grants Nos. QL20230104 and CX20240431), and the Shiyanjia Lab (www.shiyanjia.com).

Data availability

Data will be made available on request.

References

Aziz, M., Towhata, I., Yamada, S., Qureshi, M.U., Kawano, K., 2010. Water-induced granular decomposition and its effects on geotechnical properties of crushed soft rocks. Nat. Hazards Earth Syst. Sci. 10 (6), 1229–1238.
Aziz, M., Towhata, I., Irfan, M., 2016. Strength and deformation characteristics of degradable granular soils. Geotech. Test. J. 39 (3), 452–461.
Aziz, M., Mohammed, A.S., Ali, U., Saleem, M.A., Mazher, K.M., Hanif, A., Ali, U., 2024. Deep learning-based prediction of particle breakage and friction angle of water-degradable geomaterials. Powder Technol. 444, 120049.
Chen, Y., Zhang, L., Chen, Z., Liu, Z., Luo, B., Ding, X., Lu, Z., 2025. Analysis of triaxial shear properties of mudstone coarse-grained soils considering penetrating erosion effects. Transport. Geotech. 50, 101469.
Crowell, J.C., 1957. Origin of pebbly mudstones. Geol. Soc. Am. Bull. 68 (8), 993–1010.
Dai, S., He, X., Tong, C., Gao, F., Zhang, S., Sheng, D., 2023. Stability of sandy soils against internal erosion under cyclic loading and quantitatively examination of the composition and origin of eroded particles. Can. Geotech. J. 61 (4), 732–747.
Einav, I., 2007. Breakage mechanics - part I: theory. J. Mech. Phys. Solid. 55 (6), 1274–1297.
Hu, W., Yin, Z., Dano, C., Hicher, P.Y., 2011. A constitutive model for granular materials considering grain breakage. Sci. China Technol. Sci. 54, 2188–2196.
Hu, W., Xu, Q., Wang, G., Scaringi, G., McSaveney, M., Hicher, P.Y., 2017. Shear resistance variations in experimentally sheared mudstone granules: a possible shear-thinning and thixotropic mechanism. Geophys. Res. Lett. 44 (21), 11–40.
Israr, J., Aziz, M., 2019. Integrating the role of relative density on assessing internal stability of granular filters using existing geometrical methods. Arabian J. Geosci. 12 (21), 646.
Li, J., Yin, Z.Y., Cui, Y., Hicher, P.Y., 2017. Work input analysis for soils with double porosity and application to the hydromechanical modeling of unsaturated expansive clays. Can. Geotech. J. 54 (2), 173–187.
Li, S., Yang, Z., Tian, X., Xiao, Y., Li, X., Liu, X., 2021. Influencing factors of scale effects in large-scale direct shear tests of soil-rock mixtures based on particle breakage. Transport. Geotech. 31, 100677.
Li, Z., Nie, L., Xue, Y., Li, W., Fan, K., 2025. Model testing on the processes, characteristics, and mechanism of eater inrush induced by karst caves ahead and alongside a tunnel. Rock Mech. Rock Eng. 58 (5), 5363–5380.
Liu, L., Yao, Y., Luo, T., Zhou, A., 2020. A constitutive model for granular materials subjected to a large stress range. Comput. Geotech. 120, 103408.
Liu, Y., Yin, Z.Y., Wang, L., Hong, Y., 2021. A coupled CFD–DEM investigation of internal erosion considering suspension flow. Can. Geotech. J. 58 (9), 1411–1425.
Liu, Y., Wang, L., Hong, Y., Yin, Z.Y., 2022. Coupled thermo-hydro-mechanical-chemical modeling of fines migration in hydrate-bearing sediments with CFD-DEM. Can. Geotech. J. 60 (5), 701–717.
Liu, L., Jin, J., Liu, J., Cheng, W., Zhao, M., Luo, S., Wang, T., 2025. Mechanical properties of sandstone under in-situ high-temperature and confinement conditions. Int. J. Miner. Metall. Mater. 32 (4), 778–787.
Ma, G., He, X., Jiang, X., Liu, H., Chu, J., Xiao, Y., 2021. Strength and permeability of bentonite-assisted biocemented coarse sand. Can. Geotech. J. 58 (7), 969–981.
McKenna, G., Argyroudis, S.A., Winter, M.G., Mitoulis, S.A., 2021. Multiple hazard fragility analysis for granular highway embankments: moisture ingress and scour. Transport. Geotech. 26, 100431.
Peng, Y., Ding, X., Xiao, Y., Deng, X., Deng, W., 2020. Detailed amount of particle breakage in nonuniformly graded sands under one-dimensional compression. Can. Geotech. J. 57 (8), 1239–1246.
Peng, S., Rice, J.D., Zhang, W., Luo, G., Cao, H., Pan, H., 2024. Laboratory investigation of the effects of blanket defect size on initiation of backward erosion piping. J. Geotech. Geoenviron. Eng. 150 (10), 4024095.
Qian, J., Zhang, C., Zhou, W., Tang, Y., Li, J., Li, C., 2024. A thermodynamically consistent constitutive model for soil-rock mixtures: a focus on initial fine content and particle crushing. Comput. Geotech. 169, 106233.
Rasool, A.M., Aziz, M., 2020. Advanced triaxial tests on partially saturated soils under unconfined conditions. Int. J. Civ. Eng. 18 (10), 1139–1156.
Sheng, D., Yao, Y., Carter, J.P., 2008. A volume–stress model for sands under isotropic and critical stress states. Can. Geotech. J. 45 (11), 1639–1645.
Shi, J., Xiao, Y., Hu, J., Wu, H., Liu, H., Haegeman, W., 2022. Small-strain shear modulus of calcareous sand under anisotropic consolidation. Can. Geotech. J. 59 (6), 878–888.
Tang, Q., Gratchev, I., 2023. Estimation of sedimentary rock porosity using a digital image analysis. Appl. Sci. 13 (4), 2066.
Tang, H., Zhu, M., 2025. A nonlinear breakage mechanics model: from extreme entire life model to breakage evolution of limestone based on separation of Helmholtz free energy under cyclic loading. Int. J. GeoMech. 25 (2), 4024336.
Wei, H.Z., Xu, W.J., Xu, X.F., Meng, Q.S., Wei, C.F., 2018. Mechanical properties of strongly weathered rock–soil mixtures with different rock block contents. Int. J. GeoMech. 18 (5), 04018026.
Wu, M., Sun, Y., Situ, X., Wang, J., Yin, Z.Y., 2024. Computed tomography-driven analysis of particle breakage using a coupled FDM-DEM approach. Can.

Geotech. J. https://doi.org/10.1139/cgj-2024-0255.
Xiao, P., Liu, H., Stuedlein, A.W., Evans, T.M., Xiao, Y., 2019. Effect of relative density and biocementation on cyclic response of calcareous sand. Can. Geotech. J. 56 (12), 1849–1862.
Xiong, H.B., Yu, Q., Zhang, S., Tong, C.X., Lan, P., Liu, G.Q., 2021. UH model and parameter inversion for crushable sands. Chin. J. Geotech. Eng. 45 (1), 134–143 (in Chinese).
Xu, D., Zhang, Z., Qin, Y., Liu, T., Cheng, Z., 2022. Effect of particle size distribution on dynamic properties of cemented coral sand under SHPB impact loading. Soil Dynam. Earthq. Eng. 162, 107438.
Xu, D., Zhang, S., Qin, Y., 2024. Study of the micromechanical properties and dissolution characteristics of porous coral reef limestone. J. Geophys. Res. Solid Earth 129 (11), e2024JB029131.
Yang, J., Yin, Z.Y., Laouafa, F., Hicher, P.Y., 2020. Hydromechanical modeling of granular soils considering internal erosion. Can. Geotech. J. 57 (2), 157–172.
Yao, Y.P., Hou, W., Zhou, A.N., 2009. UH model: three-dimensional unified hardening model for overconsolidated clays. Geotechnique 59 (5), 451–469.
Yao, Y.P., Kong, Y.X., 2012. Extended UH model: three-dimensional unified hardening model for anisotropic clays. J. Eng. Mech. 138 (7), 853–866.
Yao, Y.P., Zhou, A.N., 2013. Non-isothermal unified hardening model: a thermo-elasto-plastic model for clays. Geotechnique 63 (15), 1328–1345.
Yao, Y.P., Niu, L., Cui, W.J., 2014. Unified hardening (UH) model for overconsolidated unsaturated soils. Can. Geotech. J. 51 (7), 810–821.
Yao, Y., Tian, Y., Gao, Z., 2017. Anisotropic UH model for soils based on a simple transformed stress method. Int. J. Numer. Anal. Methods GeoMech. 41 (1), 54–78.
Yao, Y.P., Liu, L., Luo, T., Tian, Y., Zhang, J.M., 2019. Unified hardening (UH) model for clays and sands. Comput. Geotech. 110, 326–343.
Yao, Y.P., Fang, Y.F., 2020. Negative creep of soils. Can. Geotech. J. 57 (1), 1–16.
Yao, Y., Wang, N., Chen, D., 2021. UH model for granular soils considering low confining pressure. Acta Geotech 16, 1815–1827.
Yao, Y., Li, J., Ni, J., Liang, C., Zhang, A., 2022. Effects of gravel content and shape on shear behaviour of soil-rock mixture: experiment and DEM modelling. Comput. Geotech. 141, 104476.
Yao, Y., Tian, Y., Cui, W., Luo, T., Li, S., 2024. Unified hardening (UH) model for unsaturated expansive clays. Acta Geotech 19 (6), 3655–3669.
Yu, F.W., 2017. Particle breakage and the critical state of sands. Geotechnique 67 (8), 713–719.
Zeng, L., Yu, J.L., Wen, W., 2024. Study of the uniaxial compressive strength of water-sensitive carbonaceous mudstones based on the single-particle crushing strength. Bull. Eng. Geol. Environ. 83 (3), 89.
Zhang, S., Liu, X., 2023. Theoretical, experimental, and numerical studies of flow field characteristics and incipient scouring erosion for slope with rigid vegetations. J. Hydrol. 622, 129638.
Zhao, J., Tong, H., Yuan, J., Wang, Y., Cui, J., Shan, Y., 2025a. Three-dimensional strength and deformation characteristics of calcareous sand under various stress paths. Bull. Eng. Geol. Environ. 84 (1), 61.
Zhao, Y., Lu, Z., Gedela, R., Tang, C., Feng, Y., Liu, J., Yao, H., 2025b. Performance and geocell-soil interaction of sand subgrade reinforced with high-density polyethylene, polyester, and polymer-blend geocells: 3D numerical studies. Comput. Geotech. 178, 106949.
Zheng, W., 2015. A cyclic UH model for sand. Earthq. Eng. Eng. Vib. 14 (2), 229–238.
Zhou, H., Liu, Z., Shen, W., Feng, T., Zhang, G., 2022. Mechanical property and thermal degradation mechanism of granite in thermal-mechanical coupled triaxial compression. Int. J. Rock Mech. Min. Sci. 160, 105270.
Zou, B., Pei, C., Chen, Q., Deng, Y., Chen, Y., Long, X., 2025. Progress on multi-field coupling simulation methods in deep strata rock breaking analysis. Comput. Model. Eng. Sci. 142 (3), 2457–2485.

Ling Zhang is a Professor and Doctoral Supervisor at Hunan University. She earned her Ph.D. in Civil Engineering from Hunan University in 2012. Her research focuses on innovative technologies for the treatment of special soil subgrades and the design of pile foundations in challenging and unique environments. She has led four projects funded by the National Natural Science Foundation of China (NSFC), as well as one project supported by the Hunan Provincial Excellent Young Scholars Fund. To date, she has published over 100 academic papers in core journals at home and abroad, including 42 papers indexed by SCI. Professor Zhang actively contributes to the academic community as a reviewer for several leading international journals in the field of civil and geotechnical engineering, including *Geotextiles and Geomembranes*, *Computers and Geotechnics*, *ASCE's International Journal of Geomechanics*, *Ocean Engineering*, among others.